Ferromagnetic resonance in $Ga_{1-x}Mn_xAs$ dilute magnetic semiconductors

2006 J. Phys.: Condens. Matter 18 R245

(http://iopscience.iop.org/0953-8984/18/13/R02)

INSTITUTE OF PHYSICS PUBLISHING JOURNAL OF PHYSICS: CONDENSED MATTER

J. Phys.: Condens. Matter **18** (2006) R245–R279 doi:10.1088/0953-8984/18/13/R02

TOPICAL REVIEW

Ferromagnetic resonance in $Ga_{1-x}Mn_xAs$ dilute magnetic semiconductors

Xinyu Liu and Jacek K Furdyna[1]

Department of Physics, University of Notre Dame, Notre Dame, IN 46556, USA

E-mail: xliu2@nd.edu and furdyna.1@nd.edu

Received 22 December 2005
Published 17 March 2006
Online at stacks.iop.org/JPhysCM/18/R245

Abstract

We review the phenomenon of ferromagnetic resonance (FMR) in ferromagnetic (FM) $Ga_{1-x}Mn_xAs$ semiconductor alloys and their heterostructures in thin film form. We will show that the analysis of FMR in $Ga_{1-x}Mn_xAs$ films can directly provide values of cubic and uniaxial magnetic anisotropy fields in these materials—i.e. the anisotropy associated with the natural (undistorted) zinc-blende structure and that arising from strain-induced distortion, respectively. In addition to the effects of strain, in this review we will also discuss the use of FMR to determine the effects of annealing, temperature, and doping on magnetic anisotropy. The FMR results attained on the temperature dependence of anisotropy fields (both cubic and uniaxial) provide a natural explanation of the easy-axis reorientation transition that is observed in these materials as the temperature changes. Using results observed on $Ga_{1-x}Mn_xAs$ samples where the concentration of holes is controlled either by annealing or by modulation doping, we will show that FMR also provides a convenient tool for studying the correlation between hole concentration and magnetic anisotropy. Additionally, we will show that the FMR studies of $Ga_{1-x}Mn_xAs/Ga_{1-y}Al_yAs$ heterostructures modulation doped by Be reveal that the effective g-factor of $Ga_{1-x}Mn_xAs$ is also strongly affected by the doping. The measurements of the total g-factor can in turn be used to estimate the contribution which the holes themselves make to the total magnetization of $Ga_{1-x}Mn_xAs$. Finally, we will review the results which are currently available on the FMR linewidth, including its dependence on temperature, angle of applied field, and annealing. Although the data on FMR broadening are at this time largely phenomenological, the dependence of the linewidth on hole concentrations suggests that the p–d coupling between the holes and the Mn^{2+} ions contributes significantly to the damping rate of the magnetization precession in FMR experiments on $Ga_{1-x}Mn_xAs$ films. Finally, it should be noted that—although in this review we focus on $Ga_{1-x}Mn_xAs$, because the overwhelming majority of work on FMR has been carried out on this material—the description of FMR and its

[1] Author to whom any correspondence should be addressed.

analysis presented here can be applied to thin layers of all $III_{1-x}Mn_xV$ alloys generally.

(Some figures in this article are in colour only in the electronic version)

Contents

1. Introduction

1.1. Mn in the semiconductor lattice: making semiconductors ferromagnetic

Semiconductors and magnetic materials both play essential roles in the modern electronics industry. Most electronic and optical semiconductor devices utilize the charge of electrons and holes to process information; and magnetic materials use the spin of magnetic ions for information storage. Thus—although the applications of semiconductors and magnetics have evolved independently—it appears logical to combine their properties for possible spin-electronic applications with increased functionalities [1, 2]. Coexistence of magnetism and semiconducting properties in diluted magnetic semiconductors (DMSs) has in fact already been realized by alloying the non-magnetic semiconductor host with magnetic elements as early as the 1970s [3]. In those early years, the study of DMSs and their heterostructures was primarily focused on II–VI-based materials (such as those based on HgTe, CdTe, and ZnSe),

where the valence of group II cations is identical to that of many magnetic ions, such as Mn or Co [3, 4]. The magnetic interaction in II–VI DMSs is dominated by antiferromagnetic direct exchange among the Mn spins, which results in paramagnetic, spin glass, and ultimately long range antiferromagnetic behaviour. Recent progress in doping technology of II–VI materials is, however, gradually extending these limits to broader forms of magnetism. For example, carrier-mediated ferromagnetism was recently discovered in p-type II–VI DMS heterostructures, although at the present time this only occurs at very low temperatures (the Curie temperatures T_C are typically below 2.0 K in these II–VI-based systems) [5].

On the other hand, very significant strides have recently been made in developing Mn-containing ferromagnetic III–V-based semiconductors which remain ferromagnetic to much higher Curie temperatures than those observed in their II–VI-based counterparts [6–10]. These III–V-based semiconductor ferromagnetics are fabricated in thin layer form by low temperature molecular beam epitaxy (LT-MBE). Attempts to grow such $III_{1-x}Mn_xV$ alloys were first rewarded with successful MBE growth of uniform $In_{1-x}Mn_xAs$ films on GaAs substrates [11]. The subsequent discovery of hole-induced ferromagnetic order in p-type $In_{1-x}Mn_xAs$ [12] encouraged researchers to also investigate analogous GaAs-based systems [13], ultimately resulting in the successful growth of ferromagnetic $Ga_{1-x}Mn_xAs$ [14]. Since their initial discovery, much progress has now been made in the fabrication of $Ga_{1-x}Mn_xAs$ alloys, with Curie temperatures T_C now reproducibly exceeding 150 K [15–18]. The progress made with $In_{1-x}Mn_xAs$ and $Ga_{1-x}Mn_xAs$ alloys has been subsequently followed by successful preparation of ferromagnetic III–V semiconductors $Ga_{1-x}Mn_xSb$ [19, 20] and $In_{1-x}Mn_xSb$ [21].

These III–V-based ferromagnetics taken together have already opened a number of fundamental issues in magnetism and magneto-transport, as well as in the inter-relationship between the two. Just as important, the development of these materials holds promise for integrating ferromagnetic and non-magnetic semiconductors, with an eye on developing new devices that depend—as already noted—on electron charge as well as on its spin [22]. For example, $III_{1-x}Mn_xV$ alloys have already been integrated with III–V-based non-magnetic semiconductor systems to form spin-injecting structures [23], as well as structures that allow electrical [24], optical [25], or other forms of external controls [26, 27] of the ferromagnetism exhibited by $III_{1-x}Mn_xV$ alloys.

It is generally accepted that when Mn is incorporated at the cation site in both II–VI and III–V semiconductor materials it enters the lattice as a Mn^{2+} ion, which has a half-filled d shell with an angular momentum $L = 0$ and a spin of $S = 5/2$. The exchange interaction between the Mn spin and band carriers is parametrized by exchange integrals $N_0\alpha$ and $N_0\beta$ for the conduction and valence band carriers, respectively. This parametrization scheme has been spectacularly successful in describing various optical and magnetic phenomena observed in II–VI-based paramagnetic semiconductors. In III–V semiconductors, however, Mn^{2+} ions at the group III cation site do not just serve as $S = 5/2$ magnetic moments inserted into the III–V host, but also as acceptors, so that the resulting $III_{1-x}Mn_xV$ alloys automatically contain a high concentration of holes.

One should note at this point that—in spite of various theoretical attempts and approaches [28–35]—the understanding of the origin of ferromagnetism in $III_{1-x}Mn_xV$ alloys is still rather incomplete. While the debate on this front continues, the theory of ferromagnetism based on the Zener model [36], the Ginzburg–Landau approach to the ferromagnetic phase transition in the $III_{1-x}Mn_xV$ systems, and the Kohn–Luttinger $k \cdot p$ theory of semiconductors are now rather widely accepted, since they are able to satisfactorily describe a number of magnetic properties of these materials. In this review we will also adhere to this view.

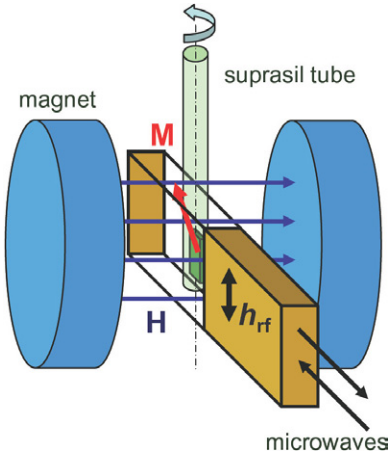

Figure 1. Schematic diagram of the EPR/FMR apparatus.

1.2. FMR: probing dynamic magnetic properties of ferromagnetic semiconductors

One of the key properties of $III_{1-x}Mn_xV$ ferromagnetic semiconductors (FMSs) is their magnetic anisotropy, since this is the basic parameter for developing future spin-based devices (e.g. spin-injectors [37] and tunnel junctions [38], as well as devices based on the giant planar Hall effect (GPHE) [39] and structures involving nano-constrictions, which exhibit giant magnetoresistance [40]). Since the ferromagnetic interaction in $III_{1-x}Mn_xV$ materials is mediated by free holes [36], the magnetic anisotropy of $III_{1-x}Mn_xV$ FMSs can therefore be directly traced to the Fermi surface anisotropy of these charge carriers, since it is the holes that determine the ferromagnetic exchange between the localized (isotropic) Mn^{2+} spins [41, 30].

Ferromagnetic resonance (FMR) is one of the most powerful experimental techniques for the study of ferromagnetic thin films [42], providing the opportunity for determining all their essential properties, including magnetic anisotropy, total magnetic moment, Curie temperature, magneto-elastic coupling coefficients, and parameters describing the relaxation of magnetization. High sensitivity, high resolution, and relatively easy set-up and sample exchange are among the advantages of the FMR experiment. In addition to reviewing the results of FMR obtained on $III_{1-x}Mn_xV$ FMSs, in this review we will take special note of how the FMR technique complements the more conventional magnetic studies to obtain information on basic magnetic properties of epitaxially grown thin $Ga_{1-x}Mn_xAs$ films.

To illustrate the capabilities of the FMR technique, we will make extensive use of FMR measurements carried out by our own group at 9.4 GHz (X-band) using a Bruker electron paramagnetic resonance (EPR) spectrometer. As shown in figure 1, in these experiments (typical of many FMR set-ups) the applied dc magnetic field is confined to the horizontal plane, and a weak microwave (rf-) field acting on the sample is vertical. The magnetic film is placed in a sample holder tube inserted into a liquid helium continuous flow cryostat, which is in turn inserted into the microwave cavity of the EPR spectrometer, the cavity itself remaining at room temperature[2]. The helium flow is driven by a small-diaphragm vacuum pump, which circulates the helium gas through the system. The under-pressure produced by the pump is sufficient to achieve temperatures down to 3.6 K.

[2] There are of course many types of FMR spectrometers, including those with the microwave cavity immersed in the cryogen. We will find it convenient to use the system just described in discussing experiments in this review because of the ease of varying the magnetic field orientation relative to the sample coordinates.

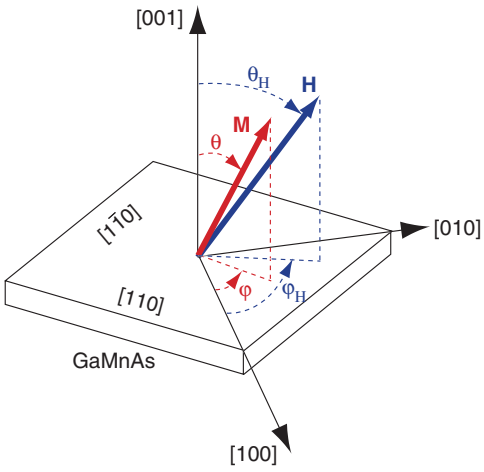

Figure 2. Coordinate system used in this review. The orientation of the applied dc magnetic field **H** is described by (θ_H, φ_H). The resulting equilibrium orientation of the magnetization **M** is given by (θ, φ).

The FMR measurement procedure is similar to nuclear magnetic resonance (NMR) and EPR [43]. One should bear in mind, however, that in the FMR measurements on $III_{1-x}Mn_xV$ films the total magnetic moment of the Mn-ion/hole complex comprising the ferromagnetism of the system precesses *as a whole* around *the resultant of all static magnetic fields* present in the system (i.e. the applied dc magnetic field, the magnetic anisotropy field, and the demagnetization fields) at the Larmor frequency ω. Since the experimental microwave frequency is fixed by the resonance frequency of the cavity (for example, our FMR experiments are carried out at 9.4 GHz), a dc magnetic field is swept as the independent variable. When the Larmor precession frequency ω coincides with the rf-frequency, a resonance takes place between the motion of the Mn-ion/hole spin complex and the microwave signal. This resonance condition manifests itself as a peak in absorption of the incident microwaves, resulting in a decrease of the quality factor (the 'Q') of the cavity. As an operational detail, one should add that it is convenient (and more precise) to observe the *derivative* of this resonant absorption—and thus all raw FMR spectra shown in this paper will be in the form of the first derivative of the absorption as a function of the applied field.

1.3. Typical sample preparation and mounting for FMR measurements

In the experimental approach just described, the sample and the sample holder need to be free from moisture in order to avoid spurious signals from condensates (particularly from oxygen at low temperatures, which is paramagnetic). To achieve this, the samples are typically cleaned with methanol and inserted into the sample tube, which is filled with helium gas and then sealed with paraffin tape. The use of Suprasil as sample holder tubes rather than quartz has been found to be advantageous, because impurities in quartz also result in spurious resonances that can complicate in the observed spectra.

When magneto-crystalline anisotropy is present, FMR spectra will depend on the orientation of the applied magnetic field with respect to the crystalline axes. In most examples which we will describe, a given $Ga_{1-x}Mn_xAs$ layer has been cleaved into three square pieces with edges along the [110] and [1$\bar{1}$0] directions, as shown in figure 2. This figure illustrates the polar coordinate system which we will use throughout this review. To preserve the desired

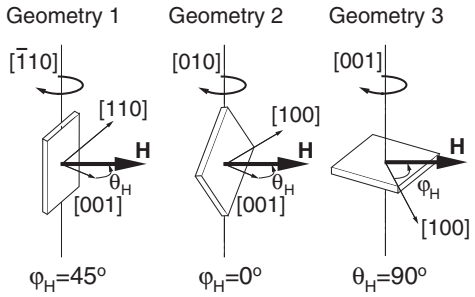

Figure 3. Three experimental configurations used in this review. The orientation of the dc magnetic field **H** (given by θ_H and φ_H) can be varied continuously in the $(1\bar{1}0)$ plane (or in the (110) plane when the [110] direction points up) (geometry 1, $\varphi_H = \pm 45°$), in the (010) plane (geometry 2, $\varphi_H = 0°$), and in the (001) plane (geometry 3, $\theta_H = 90°$). The corresponding equilibrium orientations of the magnetization **M** are given by (θ, φ).

orientation, each square piece is then cemented to a long parallelepiped of the GaAs(100) SI substrate material (the same material as that used for growth of the ferromagnetic film) in one of the three geometries shown in figure 3, and then inserted into the sample tube. With the magnetic field confined to the horizontal plane, mounting the sample with the layer plane vertical allows one to carry out magnetic resonance measurements in two basic configurations, which we will refer to as geometries 1 and 2. Specifically, mounting the specimen with the $[\bar{1}10]$ (or [110]) edge vertical (geometry 1, $\varphi_H = \pm 45°$) enables measurements with the dc field **H** in any intermediate orientation between the normal to the layer plane, **H** ∥ [001], and the in-plane orientation, **H** ∥ [110] (or **H** ∥ $[\bar{1}10]$). Similarly, when the sample is mounted so that the [010] direction—i.e. the diagonal of the square—is vertical (geometry 2, $\varphi_H = 0°$), one can map out the FMR for field orientations between the normal orientation, **H** ∥ [001], and the in-plane orientation **H** ∥ [100]. Additionally, a third configuration (geometry 3, $\theta_H = 90°$) can be used by mounting the sample with the layer plane oriented horizontally (i.e. with the [001] direction pointing up). In this configuration one can measure the angular dependence of FMR when the field is confined to the layer (i.e. to the (001) plane), including the orientations **H** ∥ [110], **H** ∥ $[\bar{1}10]$, **H** ∥ [100], and **H** ∥ [010], as well as **H** along all intermediate orientations in the layer plane. Typically, the direction of the magnetic field with respect to the crystal axes of the sample is controlled using a single-axis goniometer located on top of the microwave cavity. In this type of arrangement it is possible to rotate the sample holder through 360° with an angular precision of 0.125°.

In this review we will focus on the information obtained from the FMR field position H_R, at different temperatures and at different orientations of the applied dc magnetic field **H** relative to the crystal axes of the $Ga_{1-x}Mn_xAs$ specimen. Based on these results, we will show that FMR provides a unique way of determining the magnetic anisotropy fields and the effective g-factor of the precessing Mn-ion/hole complex.

2. Determining magnetic anisotropy by FMR

2.1. Overview of magnetic anisotropy in epitaxial $III_{1-x}Mn_xV$ layers

Because of the low solubility of Mn in bulk III–V semiconductors, $Ga_{1-x}Mn_xAs$ alloys with x sufficiently high to produce cooperative magnetic effects ($x > 0.01$) can only be achieved in layers grown by low temperature molecular beam epitaxy (LT-MBE), and thus the

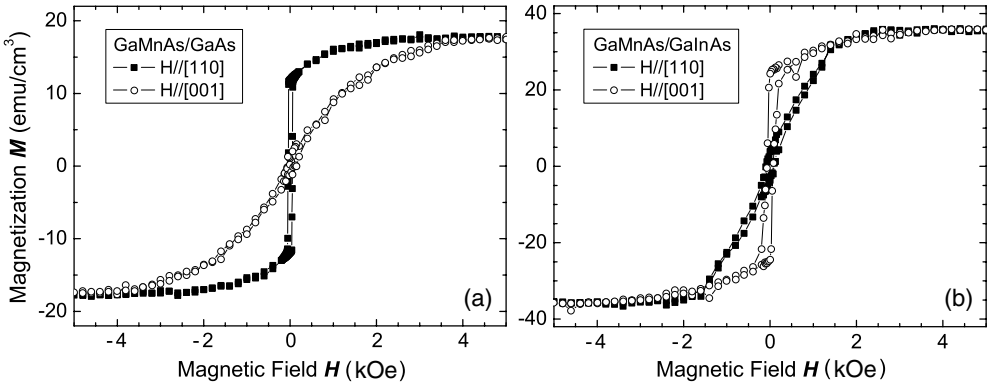

Figure 4. Magnetization M as a function of applied magnetic field H for a $Ga_{0.97}Mn_{0.03}As$ film, measured at $T = 5$ K by SQUID for $Ga_{0.97}Mn_{0.03}As$/GaAs (left panel) and $Ga_{0.97}Mn_{0.03}As/Ga_{0.85}In_{0.15}As$ (right panel). The magnetic field is applied either in the [110] or in the [001] direction. $Ga_{0.97}Mn_{0.03}As$ grown directly on a (001) GaAs substrate (left panel) is under compressive strain in the layer plane; $Ga_{0.97}Mn_{0.03}As$ grown on a $Ga_{0.85}In_{0.15}As$ buffer (right panel) is under tensile strain. Note that the easy axis is different for the two samples.

in-plane lattice constants of such layers are locked to those of their substrates. For example, x-ray diffraction (XRD) experiments reveal that $Ga_{1-x}Mn_xAs$ films grown by LT-MBE are coherently strained throughout its thickness by the underlying layers (typically GaAs or $Ga_{1-y}In_yAs$), even for films as thick as 6.8 μm [44]. Based on mean-field theory calculations, it has been shown that for $III_{1-x}Mn_xV$ films grown in the [001] direction the strain splits the heavy and light hole bands of the $III_{1-x}Mn_xV$ film, producing a uniaxial contribution to its magnetic anisotropy with the following properties: the orientation of the easy axis along the growth direction is favoured when the strain shifts the heavy holes *below* the top of the light-hole sub-band; and an in-plane easy axis occurs in the opposite circumstance [30, 41].

Experimentally, it has also been clearly confirmed that a $III_{1-x}Mn_xV$ film can be magnetized more easily along certain crystallographic directions than others. This is illustrated by figure 4, showing dc SQUID magnetization measurements carried out on 300 nm $Ga_{0.97}Mn_{0.03}As$ films under different strain conditions. The hysteresis loops for $Ga_{0.97}Mn_{0.03}As$ grown on GaAs (figure 4(a)) clearly show that the easy axis of magnetization of the $Ga_{0.97}Mn_{0.03}As$ layer is in the plane of the sample, as seen from the sharp hysteresis loop when **H** is in the sample plane. In contrast, in the case of the $Ga_{0.97}Mn_{0.03}As$ grown on a relaxed $Ga_{0.85}In_{0.15}As$ buffer layer (so that the magnetic layer under tensile strain), the easy axis is obviously normal to the layer plane, as evidenced by the sharp hysteresis loop observed when **H** is applied parallel to the [001] direction (figure 4(b)).

In the absence of strain the $III_{1-x}Mn_xV$ would only be characterized by an intrinsic cubic magnetic anisotropy, arising entirely from its zinc-blende symmetry. However, the cubic magneto-crystalline anisotropy of materials grown on substrates having a lattice parameter different from their relaxed cubic form is usually masked by the lattice mismatch effects induced by the aforementioned strain, so that the cubic anisotropy terms can most readily be identified by studying the variation of magnetization when the applied field **H** is confined to the (001) plane [45–47], as illustrated in figure 5. Figures 5(a) and (b) show magnetization curves for a $Ga_{0.97}Mn_{0.03}As$/GaAs sample at 15 and 35 K for fields along the in-plane [110], [$\bar{1}$10], [100] and [010] directions. Distinct in-plane anisotropy of the magnetization is clearly seen. At 15 K, [100] is the easy axis, with essentially full magnetic moment at remanence. Hard-axis-

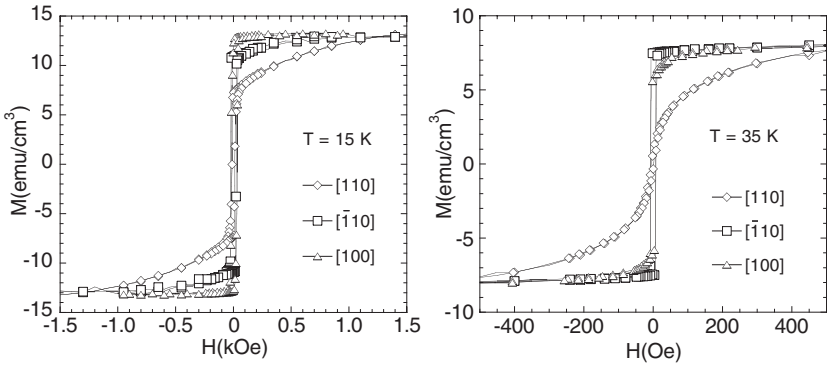

Figure 5. Magnetization curves for a $Ga_{0.97}Mn_{0.03}As$/GaAs sample at 15 K (a) and 35 K (b) with magnetic field applied along different crystallographic directions. Note the striking inequivalence of the data for [110] and [$\bar{1}$10] directions. (After Welp *et al* [45].)

like behaviour is seen for the [110] direction, with saturation occurring around 1.5 kOe. The magnetization curves for the [100] and [010] directions are identical. The distinct difference seen in the behaviour for the [110] and [$\bar{1}$10] directions is not expected on the grounds of crystal symmetry, and will be discussed in some detail later in this review. However, figure 5(b) shows that at 35 K the easy axis has switched to the [$\bar{1}$10] direction, whereas the [110] direction continues to display typical hard-axis behaviour, with essentially zero remanence, indicating that the orientation of the easy axis in the plane of a compressively strained sample can depend on temperature.

The issue of in-plane anisotropy can be further illustrated by systematic studies carried out on a series of as-grown $Ga_{1-x}Mn_xAs$/GaAs films with thicknesses ranging from 0.2 to 6.8 μm [44]. For all samples in that study one finds a clear difference between the [$\bar{1}$10] and [110] directions, i.e. a uniaxial anisotropy contribution associated with the [110] direction. It is important to note that the degree of the uniaxial anisotropy is essentially independent of the thickness of the film for the studied range of film thicknesses. Based on recent investigations on annealed-and-etched samples [48], it has been suggested that the uniaxial anisotropy could originate from a small trigonal distortion, which may be associated with the surface As dimerization, seeded by the anisotropy of the surface of the GaAs(001) substrate. This As-dimer morphology, along with the resulting trigonal distortion, then replicates itself layer by layer during the growth, leading to the uniaxial anisotropy of the film that persists throughout the entire thickness of the $Ga_{1-x}Mn_xAs$ film.

2.2. *FMR spectra of thin ferromagnetic semiconductor films*

Historically, the first experimental observation of FMR was made by Griffiths in nickel metal [49], and the initial theory of this resonance phenomenon was given by Kittel [50]. Since then, a large volume of research has been reported describing FMR in different geometries and for different classes of materials. Quantitative information on the gyromagnetic ratio, magnetic anisotropy (up to sixth order) and relaxation of magnetization in both bulk and thin film ferromagnetic materials has been obtained in these studies. FMR can thus now be considered as a well established technique, with a solid theoretical base for probing the ferromagnetic properties, that often are not accessible by other means.

For diluted magnetic semiconductor (DMS) materials in the paramagnetic state, electron paramagnetic resonance (EPR) experiments—the sister technique of FMR—have been carried

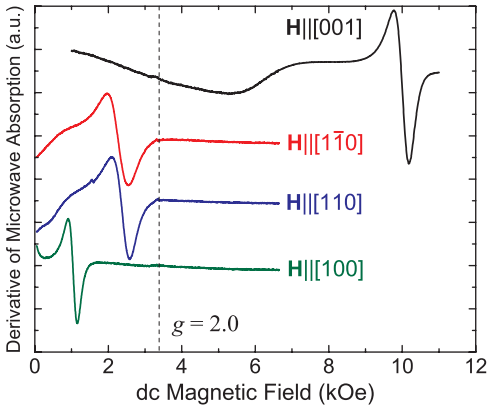

Figure 6. FMR spectra observed at $T = 4$ K for a modulation-doped $Ga_{0.94}Mn_{0.06}As/Ga_{0.76}Al_{0.24}As$:Be sample at the perpendicular (**H** ∥ [001]) and three in-plane (**H** ∥ [110], **H** ∥ [1$\bar{1}$0], and **H** ∥ [100]) configurations.

out for as long as these materials have been known [51–58]. EPR studies of bulk GaAs:Mn were also carried out, but the primary purpose of these studies was to identify the nature of the Mn centre [A^- and A^0 ($d^5 + h$)] in GaAs [59, 60]. However, when MBE-grown $III_{1-x}Mn_xV$ emerged as a material of interest, it was found that the magnetic resonance in this new material system is different. For the $Ga_{1-x}Mn_xAs$ and $In_{1-x}Mn_xAs$ epilayers with low Mn content, $x < 0.01$, only a single resonance is visible at a position corresponding to $g \sim 2.0$ [61, 62], which can still be identified as a broadened A^- resonance. But for $Ga_{1-x}Mn_xAs$ with higher Mn concentrations ($x > 0.02$), the EPR spectra become replaced by FMR spectra produced by the coherent collective precession of the coupled Mn-ion/hole complex. The earliest experiments of both EPR and FMR on a ferromagnetic $Ga_{1-x}Mn_xAs$ specimen ($x > 0.02$) were carried out by Nojiri *et al* [63], Sasaki *et al* [64], Goennenwein *et al* [65], and Balascuta *et al* [66]. These were followed by more detailed investigations of $Ga_{1-x}Mn_xAs$ and $Ga_{1-x-y}In_yMn_xAs$, accompanied by a comprehensive analysis of the FMR results [67, 68]. Moreover, recently FMR measurements have also been successfully carried out in FM $In_{1-x}Mn_xAs$ films with an in-plane easy axis [69].

In figure 6 we show typical FMR spectra (i.e. the derivative of the absorption as a function of applied magnetic field) at 4.0 K for a modulation-doped $Ga_{0.94}Mn_{0.06}As$(5.6 nm)/$Ga_{0.76}Al_{0.24}As$:Be(13.5 nm) heterostructure[3] in four basic configurations: **H** ∥ [001], **H** ∥ [110], **H** ∥ [1$\bar{1}$0], and **H** ∥ [100]. Strikingly, sharp Lorentzian-shape FMR lines are observed in all configurations (and persist up to the Curie temperature T_C), indicating strong long range ferromagnetic coherence of the Mn^{2+} spins. We find this to be remarkable, since the 5.6 nm thick $Ga_{0.94}Mn_{0.06}As$ film is approximately equivalent to only one monolayer of Mn ions randomly distributed over the plane of the specimen. Note that pronounced shifts of the FMR line are observed to fields above and below the $g = 2.00$ ($H = \omega/\gamma$) resonance position for magnetic field orientations perpendicular and parallel to the plane of the layer, respectively. Furthermore, obvious differences between FMR spectra observed in the three in-plane geometries (i.e. **H** ∥ [110], **H** ∥ [1$\bar{1}$0], and **H** ∥ [100]) are conspicuous in the figure. By their strong dependence on crystal geometry, the FMR spectra in figure 6 thus establish that magnetic anisotropy plays a major role in determining the fields at

[3] We will return to the doping issue later in the review. For the present, we use this sample series solely for illustrating the properties of FMR in very thin $Ga_{1-x}Mn_xAs$ films.

which the resonances occur [64]. The observation of sharp FMR spectra in these very thin specimens also suggests that the magnetization is nearly homogenous throughout the $Ga_{1-x}Mn_xAs$ layer, and can thus indeed be treated as a single magnetic moment precessing coherently around a dc magnetic field.

2.3. *Theoretical model of FMR: the uniform mode resonance*

As shown in the preceding section, a ferromagnet can be magnetized more easily along certain crystallographic directions than along others. One can then speak of easy, intermediate, and hard axes of magnetization. In the FMS $Ga_{1-x}Mn_xAs$/GaAs system at liquid helium temperature, for example, these correspond to [100], [110], and [001] crystallographic directions, respectively. Different orientations of **M** correspond to different free energies of the system, and differences in these energies are referred to as magnetic anisotropy energy. Magnetic anisotropy is essential not only for the fundamental understanding of the microscopic origins of ferromagnetism in FMSs, but is of central importance for applications of these materials, since it determines the direction of magnetization, coercive fields, and domain sizes. Note that there are only two microscopic sources of magnetic anisotropy energy: (a) the dipole–dipole interaction, which senses the outer shape of the sample, and (b) the spin–orbit coupling, which couples the spin to the charge (orbital) density distribution in the crystal of interest [42].

In analysing experiments carried out on FMS films (e.g. FMR experiments aimed at determining the effects of magnetic anisotropy on $Ga_{1-x}Mn_xAs$ layers), one can make use of the Stoner–Wohlfarth model [70], which assumes the ferromagnetic layer to consist of a *single homogeneous magnetic domain*. In this scheme, the free-energy density F can be expressed as the sum of three contributions when an external magnetic field is applied (see the configuration shown in figure 2): Zeeman, demagnetization, and magnetic anisotropy energies. The Zeeman energy is given by $F_{\text{Zeeman}} = -\mathbf{H}\cdot\mathbf{M} = -HM[\cos\theta\cos\theta_{\text{H}} + \sin\theta\sin\theta_{\text{H}}\cos(\varphi-\varphi_{\text{H}})]$. The demagnetization (sometimes also referred to as shape anisotropy) may, for the case of epitaxial layers corresponding to the (001) plane of interest here, be approximated by the expression describing demagnetization energy of an infinite plane: $F_{\text{shape}} = 2\pi M^2\cos^2\theta$. Finally, and most important, there is the magnetic anisotropy energy term F_{an}, which depends on the crystallographic structure of the material.

For a thin film of tetragonal symmetry (e.g. for a film of zinc-blende crystal structure such as the FMS $Ga_{1-x}Mn_xAs$ layer under a slight tetragonal distortion) in an applied magnetic field **H**, this leads to an expression for the free energy density F that can be parametrized by four anisotropy fields—$H_{2\perp}$, $H_{4\perp}$, $H_{2\parallel}$, and $H_{4\parallel}$—as shown below [42, 67]:

$$F = \tfrac{1}{2}M\Big\{-2H\left[\cos\theta\cos\theta_{\text{H}} + \sin\theta\sin\theta_{\text{H}}\cos\left(\varphi-\varphi_{\text{H}}\right)\right] + 4\pi M\cos^2\theta - H_{2\perp}\cos^2\theta - \frac{1}{2}H_{4\perp}\cos^4\theta - \frac{1}{2}H_{4\parallel}\frac{1}{4}\left(3+\cos 4\varphi\right)\sin^4\theta - H_{2\parallel}\sin^2\theta\sin^2\left(\varphi-\frac{\pi}{4}\right)\Big\}. \tag{1}$$

Here the first term describes the Zeeman energy; the second term is the demagnetizing energy (the so-called 'shape anisotropy' term); and the remaining terms represent magnetic anisotropy energy, where $H_{2\perp}$ and $H_{4\perp}$ represent the perpendicular uniaxial and perpendicular cubic anisotropy fields, respectively; $H_{2\parallel}$ and $H_{4\parallel}$ are the in-plane uniaxial and in-plane cubic anisotropy fields, respectively; and angles (θ and φ) and (θ_{H} and φ_{H}) are defined in figure 2. The anisotropy fields H_i appearing in equation (1) are defined in terms of anisotropy energies K_i as $H_i = 2K_i/M$ (e.g., $H_{4\parallel} = 2K_{4\parallel}/M$).

The value of the perpendicular uniaxial anisotropy energy $K_{2\perp}$ is determined by the lattice-mismatch-driven biaxial strain in the FMS $Ga_{1-x}Mn_xAs$ film, as would be expected from the tetragonal distortion of the $Ga_{1-x}Mn_xAs$ lattice observed in x-ray diffraction studies [44, 71]. Since epitaxy of $Ga_{1-x}Mn_xAs$ is carried out at low temperatures (typically below 300 °C), such strain can persist even beyond the critical thickness due to the relatively high thermal barrier for the formation of misfit dislocations [44]. Note that the sign of $K_{2\perp}$ will be different for compressive and for tensile strains, thus also determining the sign of $H_{2\perp}$ for these two cases. The cubic anisotropy energies $K_{4\perp}$ and $K_{4\parallel}$, on the other hand, which determine the difference in energy between the $\mathbf{M} \parallel [100]$ and $\mathbf{M} \parallel [110]$ situations, are a result of the warping symmetry of the valence band characteristic of the cubic GaAs host lattice. In the absence of any tetragonal distortion the values of $K_{4\perp}$ and $K_{4\parallel}$ should of course be equal. However, it is expected that the tetragonal distortion (such as that caused by the lattice-mismatch-induced biaxial strain in the present case) should induce a slight difference between $K_{4\perp}$ and $K_{4\parallel}$, such as one finds in the FMS $Ga_{1-x}Mn_xAs$ system and in many thin-film metallic ferromagnetic systems.

We finally discuss the in-plane uniaxial anisotropy energy $K_{2\parallel}$, which gives rise to the last term in equation (1). This term indicates that there is a (slight) physical difference in the GaMnAs system between the case when the external field is applied in the [110] and $[1\bar{1}0]$ directions, respectively. This manifests itself in differences in the two geometries observed in magnetization measurements [45, 46, 72], in magnetotransport [39, 47] and—as will be seen below—in FMR measured for the two orientations. This is surprising, because in a cubic system the two situations, $\mathbf{H} \parallel [110]$ and $\mathbf{H} \parallel [1\bar{1}0]$, are expected to be physically equivalent for a zinc-blende film in the (001) plane; and the origin of $K_{2\parallel}$ is not clear at present. Some attempts at identifying the mechanism of the effect have been made in earlier literature, and we refer interested readers to these sources [44, 73, 48]. For the purposes of the present review we will simply acknowledge that such in-plane uniaxial anisotropy is an empirical fact verified by diverse experiments in (001) GaMnAs films, and must therefore be incorporated in formulating the free energy along with the other anisotropy terms as shown in equation (1).

The time evolution of the magnetization around the equilibrium position can be estimated using the Landau–Lifshitz–Gilbert formulation, which takes into account the damping of the magnetization [74–76]:

$$-\frac{1}{\gamma}\frac{\partial \vec{M}}{\partial t} = \vec{M} \times \left(-\frac{\partial F}{\partial \vec{M}} + \vec{h}\right) - \frac{G}{(\gamma M_S)^2}\left[\vec{M} \times \frac{\partial \vec{M}}{\partial t}\right] \tag{2}$$

where $\gamma = g\frac{\mu_B}{\hbar}$ is the gyromagnetic ratio; g, μ_B, $\hbar$, G, and M_S are the spectroscopic splitting factor, Bohr magneton, Planck constant, Gilbert coefficient, and saturation magnetization; and $\vec{M}$, F, and $\vec{h}$ denote the magnetization, free energy density, and microwave magnetic field, respectively.

It is a major convenience that the resonance condition for any given field orientation can be obtained from equation (1) by solving the following equation [77, 42]:

$$\left(\frac{\omega}{\gamma}\right)^2 = \frac{1}{M_S^2 \sin^2\theta}\left[\frac{\partial^2 F}{\partial \theta^2}\frac{\partial^2 F}{\partial \varphi^2} - \left(\frac{\partial^2 F}{\partial \theta \partial \varphi}\right)^2\right], \tag{3}$$

without the need to take into account the damping of the magnetization (i.e. without the explicit knowledge of G comprising the right-hand side of equation (2)). Here ω is the angular frequency of the microwave field. For each specific orientation of the applied field (θ_H, φ_H) the equilibrium angles of the magnetization at resonance (θ, φ) are then uniquely defined by

the minimization of the free energy density with respect to θ and φ [78],

$$\frac{\partial F}{\partial \varphi} = 0; \tag{4a}$$

$$\frac{\partial F}{\partial \theta} = 0. \tag{4b}$$

Considering equations (1)–(3), the value of the applied field corresponding to the resonance condition can then be obtained from [67, 66]:

$$\left(\frac{\omega}{\gamma}\right)^2 = \left[(H_R \times a_1 + b_1)(H_R \times a_1 + b_2) - b_3^2\right]. \tag{5}$$

Here

$$a_1 = \cos\theta\cos\theta_H + \sin\theta\sin\theta_H\cos(\varphi - \varphi_H),$$

$$b_1 = -\left[4\pi M - H_{2\perp} + H_{2\parallel}\cos^2\left(\varphi + \frac{\pi}{4}\right)\right]\cos 2\theta + H_{4\perp}\frac{\cos 2\theta + \cos 4\theta}{2} + H_{4\parallel}\frac{\cos 4\theta - \cos 2\theta}{2}\frac{3 + \cos 4\varphi}{4},$$

$$b_2 = -(4\pi M - H_{2\perp})\cos^2\theta + H_{4\parallel}\sin^2\theta\left(\cos 4\varphi - \cos^2\theta\frac{3 + \cos 4\varphi}{4}\right) + H_{4\perp}\cos^4\theta - H_{2\parallel}\left\{\sin 2\varphi + \left[\cos\theta\cos\left(\varphi + \frac{\pi}{4}\right)\right]^2\right\};$$

and

$$b_3 = \tfrac{1}{2}\cos(\theta)\left(\tfrac{3}{2}H_{4\parallel}\sin 4\varphi\sin^2\theta + H_{2\parallel}\cos 2\varphi\right).$$

It will be especially important in the process of analysing FMR data to determine the resonance condition for certain high symmetry orientations. Specifically, for the orientations of **H** and **M** in the $(1\bar{1}0)$ plane (corresponding to $\varphi = \varphi_H = 45°$), which we defined as geometry 1, one finds

$$\left(\frac{\omega}{\gamma}\right)^2 = \left\{H_R\cos(\theta_H - \theta) + \left(-4\pi M + H_{2\perp} + \frac{H_{4\perp}}{2} - \frac{H_{4\parallel}}{4}\right)\cos 2\theta + \left(\frac{H_{4\perp}}{2} + \frac{H_{4\parallel}}{4}\right)\cos 4\theta\right\} \times \left\{H_R\cos(\theta_H - \theta) + \left(-4\pi M + H_{2\perp} + \frac{H_{4\parallel}}{2}\right)\cos^2\theta + \left(H_{4\perp} + \frac{H_{4\parallel}}{2}\right)\cos^4\theta - H_{4\parallel} - H_{2\parallel}\right\}, \tag{6}$$

for **H** and **M** in the (010) plane ($\varphi_H = 0°$), referred to as geometry 2, we have

$$\left(\frac{\omega}{\gamma}\right)^2 = \left\{H_R\cos(\theta_H - \theta) + \left(-4\pi M + H_{2\perp} + \frac{H_{4\perp}}{2} - \frac{H_{4\parallel}}{2} - \frac{H_{2\parallel}}{2}\right)\cos 2\theta + \left(\frac{H_{4\perp}}{2} + \frac{H_{4\parallel}}{2}\right)\cos 4\theta\right\} \times \left\{H_R\cos(\theta_H - \theta) + \left(-4\pi M + H_{2\perp} - 2H_{4\parallel} - \frac{H_{2\parallel}}{2}\right)\cos^2\theta + (H_{4\perp} + H_{4\parallel})\cos^4\theta + H_{4\parallel}\right\} - \left(\frac{H_{2\parallel}}{2}\right)^2\cos^2\theta, \tag{7}$$

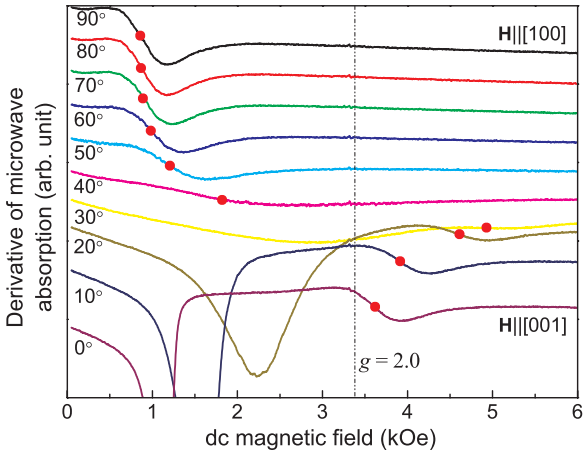

Figure 7. FMR spectra observed for the $Ga_{0.98}Mn_{0.02}As$ specimen at $T = 10$ K at various orientations θ_H for **H** between [100] and [001] directions in the (010) plane (geometry 2, θ_H from 0° to 90° in 10° increments). The full circle indicates the FMR position for the different orientations. The low field variations in the signal for $\theta_H < 30°$ arise from microwave magneto-conductivity changes in the samples.

and for **M** and **H** in the (001) plane, i.e. parallel to the film plane ($\theta = \theta_H = 90°$), which we defined as geometry 3, one obtains

$$\left(\frac{\omega}{\gamma}\right)^2 = \left\{H_R\cos(\varphi-\varphi_H) + 4\pi M - H_{2\perp} + H_{4\parallel}\frac{3+\cos 4\varphi}{4} + H_{2\parallel}\sin^2\left(\varphi-\frac{\pi}{4}\right)\right\} \times \left\{H_R\cos(\varphi-\varphi_H) + H_{4\parallel}\cos 4\varphi - H_{2\parallel}\cos\left(2\varphi-\frac{\pi}{2}\right)\right\}. \quad (8)$$

These equations allow us to obtain the values of magnetic anisotropy fields and of the effective g-factor of the Mn-ion/hole complex in the $III_{1-x}Mn_xV$ system directly from the FMR experiments. It should be noted that the angular dependence of the FMR field directly reflects the symmetry of the magnetic free energy. In particular, the orientation at which the FMR field has its lowest value corresponds to the orientation of the easy axis of magnetization.

Note that when $\varphi_H = 0°$ (geometry 2), the equilibrium angle φ of the magnetization at resonance is not always equal to φ_H due to the small but finite in-plane anisotropy field $H_{2\parallel}$. However, to simplify the analysis in deriving equation (7), we have as a first approximation ignored the possible small difference between φ and φ_H. Since the resonance field $H_R \gg H_{2\parallel}$, this assumption is quite reasonable—and is confirmed a *posteriori* by our analysis. Note also that the terms $4\pi M - H_{2\perp}$ always occur together. For this reason it is customary in calculations to lump $4\pi M - H_{2\perp}$ into a single term, which we will define as $4\pi M_{eff}$. Note finally that the microwave skin depth of $Ga_{1-x}Mn_xAs$ equals $\delta = \sqrt{2(\mu_R\mu_0\omega\sigma)^{-1}} \sim 2$ μm, a value much larger than the thickness of all investigated films. This ensures that the microwave field is uniform throughout the entire sample.

2.4. Angular dependence of the FMR field

As an illustration, we will now discuss the angular dependence of FMR for a representative $Ga_{1-x}Mn_xAs$ sample ($x = 0.02$) [79]. In figures 7 and 8 we show the observed FMR spectra, and the positions of FMR peaks for $T = 10$ K as a function of magnetic field orientation

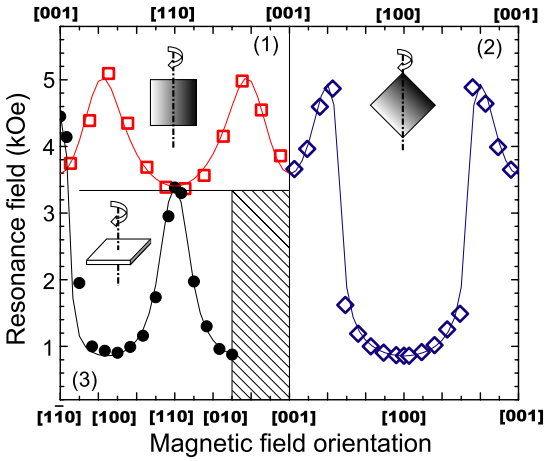

Figure 8. Angular dependence of FMR fields shown in three panels. Panel (1) corresponds to the dc magnetic field **H** and magnetization **M** in the (1$\bar{1}$0) plane, i.e. geometry 1, $\varphi_H = 45°$, panel (2) to **H** and **M** in the (010) plane, geometry 2, $\varphi_H = 0°$, and panel (3) to **H** and **M** in the (001) plane, geometry 3, $\theta_H = 90°$. The solid curves in the figure are theoretical fits to the FMR positions H_R. Note that the inequivalence of [110] and [$\bar{1}$10] is clearly seen in panel (3).

relative to the crystal axes. As shown in figure 7, FMR peaks (indicated by full circles) are observed for all field orientations. As the dc magnetic field **H** is rotated from the out-of-plane ([**H** ∥ [001], $\theta = 0°$) to the in-plane (**H** ∥ [100], $\theta = 90°$) orientation, the FMR peak position H_R clearly shifts from 1 to 5 kOe, then quickly decreases to 3.6 kOe. The FMR field positions H_R for this geometry—obtained from the experimental curves after subtracting the background—are plotted in figure 8 in panel (2). The strong dependence of the FMR spectra on crystal geometry seen in figure 8 establishes the unambiguous role of magnetic anisotropy in determining the fields at which the resonances occur.

In figure 8 there are three panels (1, 2, and 3) displaying the resonance field H_R as a function of applied field orientation, each panel corresponding to one of the three geometries described in section 1.3. Strikingly, as shown in panel (1), the angular dependence of H_R for geometry 1 is dominated by a fourfold symmetry (arising from the cubic anisotropy contribution). Similar symmetry characteristics are also present (though less obvious) in panel (2), corresponding to the second out-of-plane configuration (geometry 2). We attribute the observed symmetry of the FMR positions to the competition between the cubic ($H_{4\perp}$) and the uniaxial ($H_{2\perp}$) anisotropies [79]. From such behaviour one can infer that at low temperatures the angular dependence of H_R is dominated by the cubic anisotropy field ($H_{4\perp} > H_{2\perp}$). At the same time one should note that the lowest resonance field is observed when **H** lies in the film plane and parallel to the [100] direction ($\theta_H = 90°$, $\varphi_H = 0°$). This indicates that the easy axis of this $Ga_{1-x}Mn_xAs$ ($x = 0.02$) sample is along the [100] or the [010] direction at this temperature. Panel (3) in figure 8, which shows the angular dependence of H_R for **H** in the (001) plane, is particularly interesting for two reasons. First, it reveals that the magnetic in-plane anisotropy (which we attribute to the cubic anisotropy term $K_{4\parallel}$) is quite strong. The origin of this behaviour can be ascribed to the physical difference between the [100] and [110] orientations in the (001) plane. Second, it is evident that the symmetry of the FMR position is not exactly fourfold in the (001) plane, but that a small difference exists between H_R for **H** applied along the [110] and [1$\bar{1}$0] directions (which we attribute to the uniaxial magnetic anisotropy term $K_{2\parallel}$) [67].

We now use the FMR data shown in figure 8 to obtain the magnetic anisotropy field as follows: we first analyse the in-plane data in panel (3) via equation (8) by assuming that $g = 2.00$. This gives us approximate values of $4\pi M_{\rm eff}$, $H_{4\parallel}$ and $H_{2\parallel}$, which we use as starting parameters to carry out a weighted nonlinear least squares fit (using equations (6) and (7)) to the FMR positions shown in panels (1) and (2) of figure 8, allowing the three parameters (g, $4\pi M_{\rm eff}$, and $H_{4\perp}$) to vary. Using the values obtained by this procedure as input parameters for the next iteration, we return to the in-plane data to obtain $4\pi M_{\rm eff}$, $H_{4\parallel}$ and $H_{2\parallel}$ by using the new value of g. We iterate these two steps until optimal fitting is achieved and all five parameters ($4\pi M_{\rm eff}$, $H_{4\perp}$, $H_{4\parallel}$, $H_{2\parallel}$, and g) converge and remain unchanged in subsequent iterations.

For the specific case shown in figure 8, the final five parameters are $4\pi M_{\rm eff} = 2083 \pm 64$ Oe, $H_{4\perp} = 1826 \pm 78$ Oe, $H_{4\parallel} = 1985 \pm 71$ Oe, $H_{2\parallel} = -608 \pm 80$ Oe, and $g = 1.87 \pm 0.02$. One can see the excellent fits which have been obtained in this way for all data points, as shown by the solid theoretical curves in figure 8. Note that the cubic anisotropy field $H_{4\perp}$ is quite large. We attribute this prominence of $H_{4\perp}$ to the small value of the in-plane compressive strain in the material due to the small Mn concentration ($x = 0.02$) in the specific sample under discussion. One should note that an effective g factor obtained in this analysis is smaller than the g value of 2.00 characteristic of isolated Mn^{2+} ions. This can only be attributed to a contribution from the magnetic moment of the holes to the collective FMR precession of the coupled Mn^{2+}/hole system [80].

In summary, the FMR data for this $Ga_{1-x}Mn_xAs$ ($x = 0.02$) film and its analysis just presented illustrate the importance of magnetic anisotropy fields, both uniaxial and cubic. The reduction of the collective g-factor obtained by the analysis also illustrates that the localized Mn^{2+} ions and the free holes jointly constitute a coupled system which precesses in unison together at the FMR frequency, that is different than the Larmor frequency of the Mn^{2+} ions.

2.5. *Spin wave resonances in ferromagnetic semiconductors*

The FMR resonance mode discussed above corresponds to the spatially uniform precession of **M**, i.e., at any instant of time during their motion all magnetic moments are parallel over the entire sample. In the language of spin waves this type of mode can be regarded as a spin wave with the wave vector $k = 0$. This is, however, only a limiting case, since in principle the magnetization within the sample can depend on both space **r** and time t, $\mathbf{M} = \mathbf{M}(\mathbf{r}, t)$, due to the presence of magnons excited either thermally [81] or by some other input of energy. In thin films certain magnons from the continuum of magnon excitations can then be selectively 'amplified' when they satisfy standing waves (in a manner analogous to Fabry–Perot resonances), the 'selection' depending on the boundary conditions of the film; and those magnons selected by the film geometry can in turn be observed as additional absorption peaks. We will refer to such peaks as spin wave resonances (SWRs), which provide valuable information of the exchange energy [74]. In such a case the local moments are no longer parallel inside the sample and restoring torques due to exchange interaction and internal magnetic dipolar interactions have to be included in the analysis, resulting in effect in $k \neq 0$ excitations.

The observation of $k \neq 0$ SWRs that accompany the FMR spectra have been reported by several groups [82, 83]. In this section we will focus on the detailed description of SWRs in $Ga_{1-x}Mn_xAs$ films, and on how these excitations depend on film thickness, magnetization, and temperature. We illustrate this by SWR results reported in [82] for three $Ga_{1-x}Mn_xAs$ films with different thicknesses (100, 150, and 200 nm). The Mn concentration x of the three samples used in that study was determined by x-ray diffraction to be $x = 0.076$ and their Curie temperature measured by SQUID was 65 K.

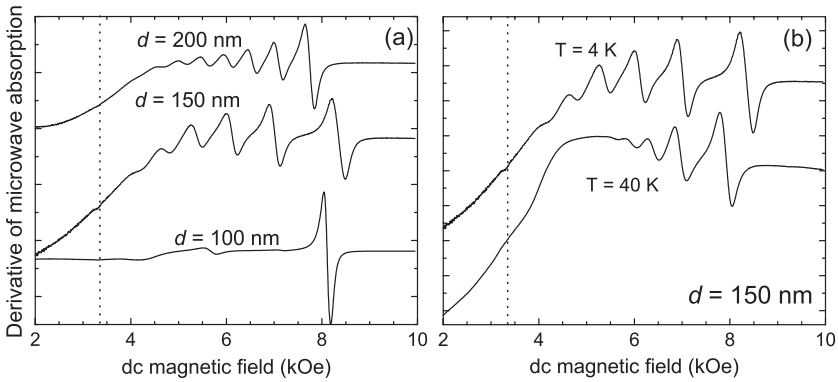

Figure 9. The derivative of the spin wave resonance (SWR) absorption as a function of applied external magnetic field: (a) SWR in $Ga_{0.924}Mn_{0.076}As$ films with three different thicknesses at 4 K; (b) SWR for 150 nm $Ga_{0.924}Mn_{0.076}As$ film measured at 4 and 40 K. The dotted line indicates the resonance position for $g = 2.00$. (After Sasaki *et al* in [82].)

SWRs were observed in this series of samples at various temperatures for **H** applied normal to the layer plane (**H** ∥ [001]). Figure 9 shows SWR spectra at 4 K for all three samples and for the 150 nm thick sample at 40 K. In the spectra observed for all samples the uniform FMR mode line (i.e. the $k = 0$ spin wave resonance) seen at around 8 kOe is accompanied by a series of SWRs at lower fields. It is important to note that—since such resonances represent a standing wave of magnetization due to the interference of spin waves reflected at the sample interfaces—the very presence of SWRs indicates that the magnetic order is coherent (i.e. long range) across the entire sample. Note that a series of such SWR modes is observed in the samples—particularly in the 200 nm thick film, which shows as many as seven SWR resonances. As seen in figure 9(a), the separation between the SWR modes increases as the film thickness is reduced.

One should also note that the separations between the successive SWR modes decrease as we increase the temperature, as shown in figure 9(b). Since the magnetization decreases with increasing temperature, we ascribe the observed change in the SWR separations as resulting either from the gradual reduction of the magnetization or from the changes in magnetic anisotropy fields that result from increasing the temperature.

Surprisingly, the SWRs reported in [82] exhibit a somewhat unusual behaviour: the fields H_n at which successive SWR modes are observed vary linearly with n, ($H_n \sim n$). Goennenwein *et al* [83] report a qualitatively similar SWR spectra, but in their case H_n is seen to progress as $n^{2/3}$. One should note that *both* results are in qualitative disagreement with the original Kittel pinning model for thin ferromagnetic films [84], which predicts that for a homogeneous layer the resonance field H_n of the nth mode should be proportional to $\sim n^2$. The origin of the anomalous SW dispersion has been attributed to the magnetic properties of $Ga_{1-x}Mn_xAs$ thin films and to the nature of pinning of the SWs at the sample boundaries. Thus, in order to explain the anomalous SW dispersion, it is necessary to allow the magnetic parameters inside the film to depend on the distance from the interface. In principle, an inhomogeneity in the profile of either magnetization, spin stiffness, or magnetic anisotropy could all result in the observed anomaly. However, the experimental and theoretical analyses [83, 85] point toward a gradient in uniaxial anisotropy and/or spin stiffness rather than a variation of the value of the magnetization itself as the cause of the observed n dependence. Variation of the uniaxial magnetic anisotropy with either a linear [83] or a quadratic [85] dependence on the distance z

from the $Ga_{1-x}Mn_xAs$/GaAs interface has been invoked by different investigators to explain their experimental results, indicating that more extensive experiments on this phenomenon are still needed in order to draw definitive conclusions as to the causes of the SWR progression observed in $Ga_{1-x}Mn_xAs$ layers.

3. FMR study of the effects of hole concentration in $Ga_{1-x}Mn_xAs$

3.1. Fabrication of samples with varying hole concentration by modulation doping

It is now generally accepted that in the $III_{1-x}Mn_xV$ systems the local Mn ions and the holes form one 'global' complex bound together by strong magnetic exchange coupling [86]. To understand magnetic phenomena in $III_{1-x}Mn_xV$ materials—such as the magnetic interlayer interaction [87], the formation of magnetic domains [45], domain wall effects [88], reorientation of the easy axis of magnetization [89], etc—it is therefore essential to investigate the correlation between magnetic properties and the concentration of holes p in these systems. It has recently been found that doping $Ga_{1-y}Al_yAs$ barriers in $Ga_{1-x}Mn_xAs/Ga_{1-y}Al_yAs$ heterostructures by Be acceptors leads to an increase of p in the $Ga_{1-x}Mn_xAs$ layer, and thus also to a significant increase in its Curie temperature T_C [90]. Such modulation-doped structures then provide a uniquely valuable opportunity for investigating hole-dependent physical properties of $Ga_{1-x}Mn_xAs$, because one can vary p in these systems without disturbing the Mn concentration within the magnetic layer. This feature is extremely important, because in 'normal' $III_{1-x}Mn_xV$ layers there exists a strong correlation between the Fermi energy and Mn incorporation during the growth, so that changes in p automatically lead to changes in the effective Mn concentration x, making it difficult to separate the effect of the holes from those of Mn [91].

To achieve modulation doping of $Ga_{1-x}Mn_xAs$ without disturbing the Mn concentration—a feature whose importance has been brought up in the preceding paragraph—the authors of [80] have grown a series of $Ga_{1-x}Mn_xAs/Ga_{1-y}Al_yAs$ heterostructures ($x = 0.06$, $y = 0.24$) by the procedure described below. Prior to growing the actual structure, a 450 nm GaAs buffer layer was deposited by MBE at 590 °C on semi-insulating (001) GaAs substrate, followed by 3 nm of GaAs grown at 210 °C. A $Ga_{1-x}Mn_xAs/Ga_{1-y}Al_yAs$ heterostructure was then deposited at 210 °C. A series of samples consisting of 5.6 nm of $Ga_{1-x}Mn_xAs$ followed by a 13.5 nm $Ga_{1-y}Al_yAs$ barrier were grown in this manner. The barriers were modulation-doped with Be at a distance of 1 ML away from the $Ga_{1-x}Mn_xAs$. In preparing specimens with different doping levels, the Be flux was kept constant during the growth, but the thickness of the doped region d_{Be} was varied: $d_{Be} = 0$ (undoped control sample), 5.3, and 13.2 nm. From SQUID measurement, all three specimens showed similar values of remanent in-plane magnetization at low temperatures (around 30 emu cm^{-3} at $T = 5$ K). Furthermore, the magnetization data obtained by SQUID also show an unambiguous increase of T_C as the degree of modulation doping is increased: $T_C = 72$, 85, and 95 K for the three studied samples, respectively.

3.2. Determination of effective g-factor of the Mn-ion/hole complex from FMR

In order to determine the magnetic anisotropy parameters in this series of samples, the values of FMR fields H_R were first analysed for the three high symmetry directions (i.e. $\mathbf{H} \parallel$ [100], [110], and [001]), following the procedure described in [67].[4] To simplify the analysis, the

[4] Note, however, that in [67] the in-plane magnetic uniaxial anisotropy was also included, while in the present samples this anisotropy is insignificantly small, and is therefore ignored.

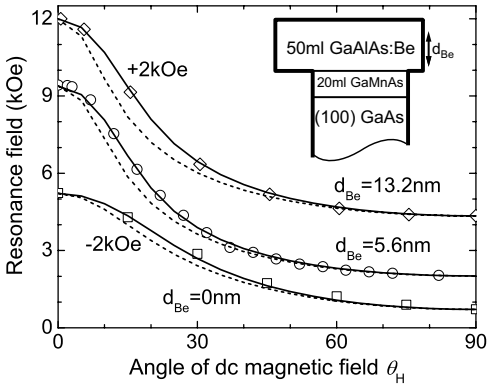

Figure 10. Angular dependence of FMR positions at 4.0 K for **H** in the $(1\bar{1}0)$ plane (geometry 1, $\varphi_H = 45°$) for an undoped and two modulation-doped $Ga_{0.94}Mn_{0.06}As/Ga_{0.76}Mn_{0.24}As$ heterostructures. Dashed curves show theoretical fits obtained for $g = 2.00$, $H_{4\perp} \neq 0$. The solid curves are fits obtained for $H_{4\perp} = 0$ and (top to bottom) $g = 1.80$, 1.87, and 1.92. Inset: schematic plot of the energy band structure of the studied heterostructures.

small in-plane uniaxial anisotropy field $H_{2\parallel}$ associated with the difference between the $[1\bar{1}0]$ and [110] axes was ignored in the calculation [44]. An independent determination of the g-factor and the three anisotropy fields $H_{2\perp}$, $H_{4\parallel}$, and $H_{4\perp}$ could not be achieved from the values of H_R for these three orientations without additional information, since there are four variables but only three equations (those corresponding to FMR observed for **H** parallel to [100], [110], and [001]). To reduce the number of variables (i.e. fitting parameters), the value of $g = 2.00$ of the individual Mn^{2+} ions was therefore assumed in the first step of the calculation, as was done in [67]. This assumption gave the angular variation of H_R shown by the dashed curves in figure 10. The dashed curves clearly depart from the data (see figure 10), indicating that the assumption of $g = 2.00$, while close, is not valid. On the other hand, we note that—due to the large in-plane compression of the $Ga_{1-x}Mn_xAs$ ($x = 0.06$) film—the effect of the cubic $H_{4\perp}$ term is expected to be completely overshadowed by $H_{2\perp}$, and may therefore be neglected in the samples under consideration. Using this approach in their iterative process, the authors of [80] assumed that $H_{4\perp} = 0$, treating g, $H_{4\parallel}$, and $H_{2\perp}$ as fitting variables. With this approach, an excellent fit to the angular variation of H_R is obtained, as shown by the solid curve in figure 10.

It should be mentioned that one can obtain the effective anisotropy parameters and the g-factor in a self-consistent way by applying a recursive iterative fitting procedure to the angular-dependent FMR results already described in section 2.4, if one can determine $H_{4\parallel}$ with sufficient accuracy [42]. The authors of [80] have therefore used the above results (based on assuming $H_{4\perp} = 0$) as starting parameters to carry out a weighted nonlinear least squares fit to FMR positions for all values of θ_H in both the $(1\bar{1}0)$ and the (010) plane, allowing *all four* parameters (g, $H_{4\parallel}$, $H_{2\perp}$, and $H_{4\perp}$) to vary. The effective g-factors obtained by this method for the three specimens with progressively increasing hole concentration are $g = 1.92 \pm 0.04$, 1.87 ± 0.03, and 1.80 ± 0.02, respectively. The result also confirms the assumption that $H_{4\perp}$ can be neglected as a first approximation. Indeed, $H_{4\perp}$ turns out to be much smaller than the fitting error.

It is clear from figure 10 that the contribution of the holes to the g-factor increases is enhanced as hole concentration increases (i.e. the fits depart further from the $g = 2.00$) as the doping level increases. One should note here that modulation-doped samples used in [80] provide an ideal tool for tracking the effect of holes on magnetic parameters in

$III_{1-x}Mn_xV$ alloys. This arises from the fact that the concentration of Mn (both substitutional and interstitial) is the same in all samples, because the deposition of the modulation-doped $Ga_{1-y}Al_yAs$:Be layer *after* the $Ga_{1-x}Mn_xAs$ layer has been grown (as described in section 3.1) does not affect the composition of the $Ga_{1-x}Mn_xAs$ layer that is already in place. The observed changes for all three samples can thus only be ascribed to changes in the hole concentration.

3.3. *Contribution of holes to the magnetization*

The effect of holes on the g-factor of the precessing assembly seen in figure 10 can be understood as follows. The total magnetization of $Ga_{1-x}Mn_xAs$ has two components: a contribution from the Mn^{2+} ions (or, more precisely, from the Mn^{2+}_{Ga} ions that are not magnetically compensated by pairing with Mn interstitials Mn_I) arising from their pure-spin magnetic moments $\mu_{Mn} = 5.0\ \mu_B$ (that corresponds to $g_{Mn} = 2.00$) and the contribution of the magnetic moments of the holes μ_h, which include both the spin and the orbital components. We must thus account for the presence of two magnetically coupled sublattice magnetizations, $M_{Mn} = n_{Mn}\mu_{Mn}$ and $M_h = p\mu_h$, where n_{Mn} and p are the effective concentrations of Mn^{2+} and of the holes. To describe the coherent precession of such a coupled system, the g-factor that is implicitly present in equations (5)–(8) through the relation $\gamma = g\mu_B\hbar^{-1}$ must be understood as an *effective* g-factor, g_{eff}, defined by [92, 93]

$$\frac{n_{Mn}\mu_{Mn} + p\mu_h}{g_{eff}} = \frac{n_{Mn}\mu_{Mn}}{g_{Mn}} + \frac{p\mu_h}{g_h}, \tag{9}$$

where g_{Mn} and g_h are the g-factors corresponding to the Mn^{2+} and hole sublattices. In order to determine the magnetization of the hole sublattice from equation (9), one should know how the spins of the Mn ions couple with the spins of the holes, i.e. the sign of the p–d exchange integral $N_0\beta$.

Despite its fundamental importance, the reader should note that various authors have reported widely different results for $N_0\beta$ for the $Ga_{1-x}Mn_xAs$ system, that vary in value—*and even in sign*—over the range from +2.5 eV (ferromagnetic exchange) [94, 61, 95] to −1.2 eV (antiferromagnetic exchange) [30, 96, 97]. However, it is essential to note that—while the different values and signs of $N_0\beta$ lead to different magnitudes of μ_h in equation (9)—both solutions indicate that the alignment of magnetic moments of the Mn^{2+} ions relative to that of the holes is antiferromagnetic, pointing to the fact that the magnetization of the hole 'sublattice' acts to reduce the overall magnetization of the collective Mn/hole system. As a result, the magnetic moments (not spins)[5] of the Mn ions and of the holes are *antiferromagnetically* coupled together, and the 'global' Mn-ion/hole complex may then effectively be viewed as a *ferrimagnetic* system. The above finding confirms that the magnetization of the hole subsystem modifies the precession dynamics of the $Ga_{1-x}Mn_xAs$ magnetization as a whole. In particular, for the most highly doped sample in [80] the magnitude of the magnetic contribution of the holes M_h was estimated to be of the order of 10% of the total magnetization M_{total}, reducing the total magnetization by approximately that amount.

The fact that holes in the $Ga_{1-x}Mn_xAs$ system contribute a finite magnetization has been predicted by many theoretical investigations [30, 98]. For example, by considering the diamagnetic contribution from Landau currents associated with the spin–orbit interaction, Dietl *et al* suggested that the magnetization of the free holes is opposite to the magnetization of the Mn^{2+} sub-lattice in $Ga_{1-x}Mn_xAs$ [30]. However, experimentally it is hard to determine the

[5] This distinction needs to be made because the contribution of holes to the magnetization is determined by how their magnetic moments align themselves with the moments of the Mn^{2+} ions; and magnetic moments of holes contain not only a spin, but also an orbital component.

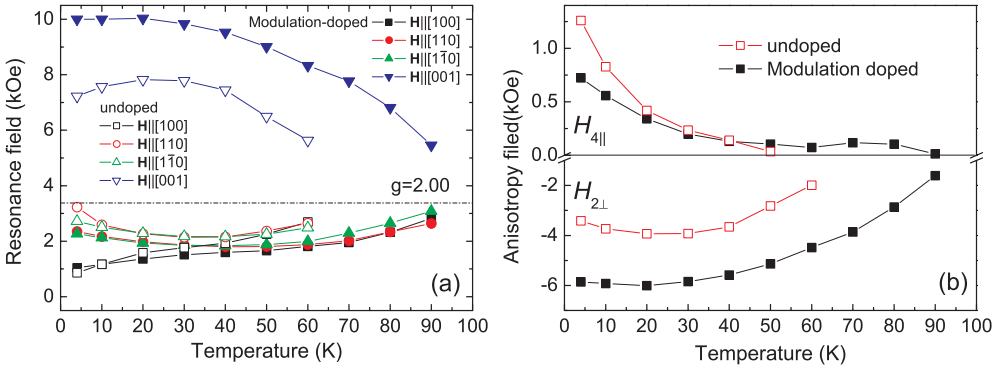

Figure 11. Temperature dependence of the FMR results for undoped (open symbols) and modulation-doped (solid symbols) $Ga_{0.94}Mn_{0.06}As/Ga_{0.76}Mn_{0.24}As$ heterostructures. (a) FMR positions observed for the four basic orientations of **H**. (b) Top and bottom panels show cubic and uniaxial anisotropy fields, $H_{4\|}$ and $H_{2\perp}$, respectively, for the two samples.

hole contribution to the total magnetization **M** using dc magnetization measurements, primarily due to the uncertainty of the effective Mn concentration (given the fact that Mn makes a much larger contribution to **M**). Magnetization measurements, however, do definitely show that there is a magnetization deficit in the $Ga_{1-x}Mn_xAs$ system [99]. While there are several mechanisms which can cause such deficit (removal of Mn from Mn_{Ga} to Mn_I sites; Mn_{Ga}–Mn_I pairing; and formation of Mn-based precipitates), the present FMR results indicate that such a deficit can also in part be attributed to the negative contribution of the holes to the total value of **M**. It should therefore be noted in this connection that in modulation-doped heterostructures one can obtain significantly larger free hole concentrations than in 'normal' $Ga_{1-x}Mn_xAs$, making these systems especially well suited for studying the effect of the holes on the overall magnetization of this alloy.

3.4. FMR studies of the dependence of magnetic anisotropy on hole concentration

We have already argued that measurements of FMR enable one to determine the temperature dependences of both magnetic anisotropy fields and of the g-factor in ferromagnetic $Ga_{1-x}Mn_xAs$ films up to their Curie temperatures T_C. As an illustration these quantities, obtained using the four basic FMR geometries (i.e. $\mathbf{H} \parallel [001]$, $\mathbf{H} \parallel [110]$, $\mathbf{H} \parallel [1\bar{1}0]$, and $\mathbf{H} \parallel [100]$) by assuming $H_{4\perp} = 0$ [80], are compared in figure 11 for undoped (open symbols) and for the most highly doped sample (solid symbols). As shown in figure 11(a), when **H** is perpendicular to the film, FMR occurs above the $g = 2.00$ resonance field (horizontal dash–dotted line), and for in-plane **H** orientations the resonance appears below that field position. Shifts from the dash–dotted line gradually decrease—and eventually vanish—as one approaches T_C. But clearly the modulation-doped sample studied in [80] has a much stronger shift (to our knowledge the strongest shift observed in any $III_{1-x}Mn_xV$ samples studied by FMR) than the undoped sample when **H** is normal to the film. This indicates a large increase of magnetic anisotropy due to the doping.

Figure 11(b) illustrates several basic features of the dependence of magnetic anisotropy on temperature and on the free hole concentration. First, we note that the cubic anisotropy fields decrease very rapidly with increasing temperature, while $H_{2\perp}$ drops off much more slowly. Second, the increase in doping unambiguously increases the perpendicular uniaxial anisotropy field $H_{2\perp}$, while reducing the in-plane cubic field $H_{4\|}$. These observations are consistent with

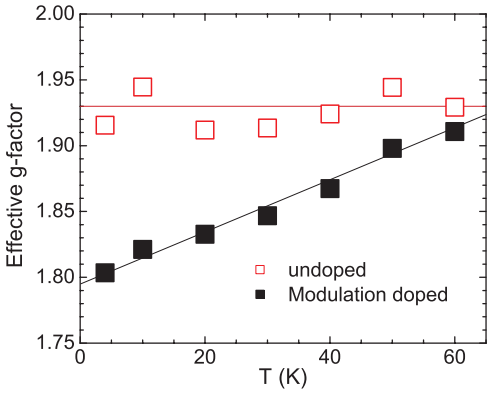

Figure 12. Temperature dependence of the effective g-factors for undoped (open symbols) and modulation-doped (solid symbols) $Ga_{0.94}Mn_{0.06}As/Ga_{0.76}Mn_{0.24}As$ heterostructures. Solid lines are guides for the eye.

theoretical calculations predicting changes of magnetic anisotropy with hole concentration, although at this point the agreement is only qualitative.

Finally, in figure 12 we plot the g-factor obtained from the analysis for the doped and the undoped specimens. For the doped sample the g-factor shows a clear tendency to decrease for temperatures below ∼50 K. While the values of the g-factor shown in figure 12 are only approximate, the low temperature decrease of this parameter in modulation doped samples may reflect the fact that larger numbers of hole spins *from holes in the* $Ga_{1-y}Al_yAs$ *barrier* will couple to Mn^{2+} spins in the $Ga_{1-x}Mn_xAs$ layer as the temperature decreases, thus increasing the effect of Landau diamagnetism on the overall magnetization.

4. Effects of strain and annealing on magnetic anisotropy measured by FMR

4.1. The effect of strain

As shown in the preceding section, FMR complements the more conventional magnetic studies of ferromagnetic films by its ability to directly determine magnetic anisotropy parameters [42]. Here we show that one can take advantage of this technique to obtain magnetic anisotropy information in $Ga_{1-x}Mn_xAs$ films under various strain conditions (the SQUID data attained on these films have been shown in section 2.1). We will illustrate this by mapping out the FMR condition data for differently strained 300 nm $Ga_{0.97}Mn_{0.03}As$ films as a function of magnetic field orientation relative to the crystal axes, as described in [67]. The observed FMR field positions obtained for the $Ga_{0.97}Mn_{0.03}As/GaAs$ sample are shown in figures 13(a) and (b), and those for $Ga_{0.97}Mn_{0.03}As/Ga_{0.85}In_{0.15}As$ are in figures 13(c) and (d). These FMR measurements were carried out in geometries 1 and 3 (i.e. **H** in the $(1\bar{1}0)$ plane and **H** in the (001) plane), corresponding to the upper (figures 13(a) and (c)) and lower panels (figures 13(b) and (d)) of figure 13, respectively. We note parenthetically that figure 13(c), $\theta_H = 0°$, provides a dramatic illustration of the decisive role played by magnetic anisotropy in positioning FMR: if K were zero, **H** applied perpendicular to the ferromagnetic layer would *never* give FMR below the $g = 2.00$ resonance position (i.e. below 3.38 kOe in the case of figure 13).

Note that the lowest resonance field for the $Ga_{0.97}Mn_{0.03}As/GaAs$ sample (figures 13(a) and (b)) is observed when **H** lies in the film plane and is parallel to the easy axis—the [100] direction ($\theta_H = 90°$, $\varphi_H = 0°$ as defined in figure 2). We attribute this to the

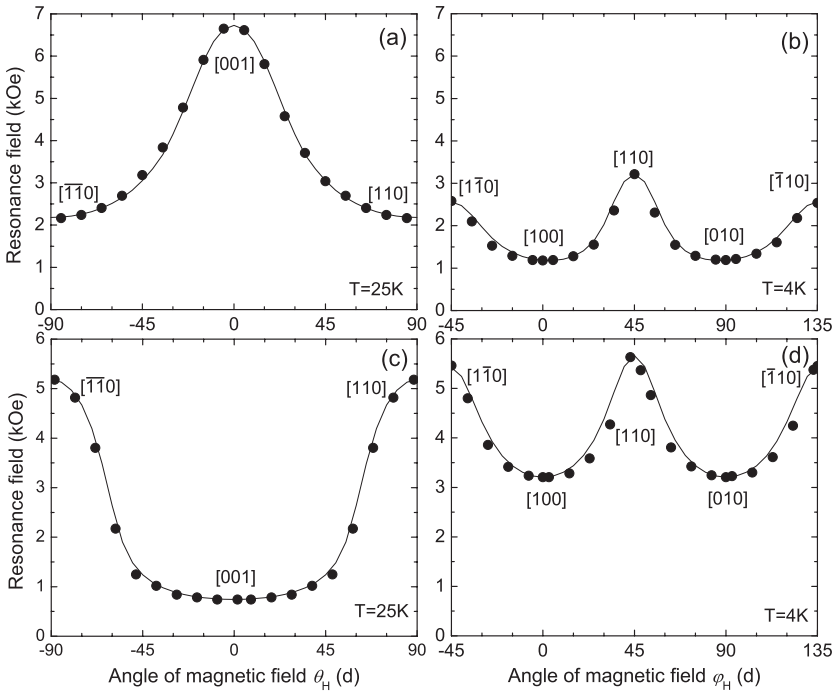

Figure 13. Angular dependence of FMR fields for a $Ga_{0.97}Mn_{0.03}As/GaAs$ sample ((a), (b)) and a $Ga_{0.97}Mn_{0.03}As/Ga_{0.85}In_{0.15}As$ sample ((c), (d)). (a), (c) dc magnetic field **H** and magnetization **M** in the $(1\bar{1}0)$ plane (geometry 1, $\varphi_H = 45°$); (b), (d) **H** and **M** in the (001) plane (geometry 3, $\theta_H = 90°$). The solid curves in the figure represent the positions of H_R calculated theoretically.

fact that $H_{2\perp}$ $(2K_{2\perp}/M)$ for this compressively strained sample is negative. Strikingly, in figures 13(c) and (d) the full angular dependences of the resonance field H_R for the $Ga_{0.97}Mn_{0.03}As/Ga_{0.85}In_{0.15}As$ film measured under the same conditions reveal that the reversal of the sign of the strain leads to a large *positive* $H_{2\perp}$ $(2K_{2\perp}/M)$, which counteracts the demagnetizing field, thus shifting the FMR position *downward* (i.e. below the $g = 2.00$ resonance field) when the magnetic field is applied normal to the plane. Furthermore, figure 13(d) shows that there is also a strong fourfold in-plane anisotropy field $H_{4\parallel}$, and again a very small but unmistakable planar twofold uniaxial anisotropy field $H_{2\parallel}$. The solid curves in figure 13 represent the positions of H_R calculated theoretically.

The above measurements of FMR show unambiguously that magnetic anisotropy plays a decisive role in determining the resonance spectrum of epitaxially grown $Ga_{1-x}Mn_xAs$. Since the crystal structure of epitaxial $Ga_{1-x}Mn_xAs$ layers is slightly tetragonal due to the distortion of its relaxed cubic structure by lattice mismatch with the substrate, it is expected that the magnetic anisotropy of this material will be dominated by uniaxial anisotropy for large Mn concentrations. Uniaxial anisotropy fields $H_{2\perp}$ $(2K_{2\perp}/M)$ as large as 4000 Oe have indeed been observed in samples with high Mn concentrations [67], and even larger values can probably be induced by greater lattice mismatches than those in the samples investigated to date. As already revealed by the positions of FMR observed for $Ga_{0.97}Mn_{0.03}As/GaAs$ and $Ga_{0.97}Mn_{0.03}As/Ga_{0.85}In_{0.15}As$, respectively, the sign of the $H_{2\perp}$ $(2K_{2\perp}/M)$ term is determined by whether the strain in the layer plane is tensile or compressive. Note, however, that the cubic (fourfold) anisotropy fields are also very large in $Ga_{1-x}Mn_xAs$ (of the order of 2000 Oe), as

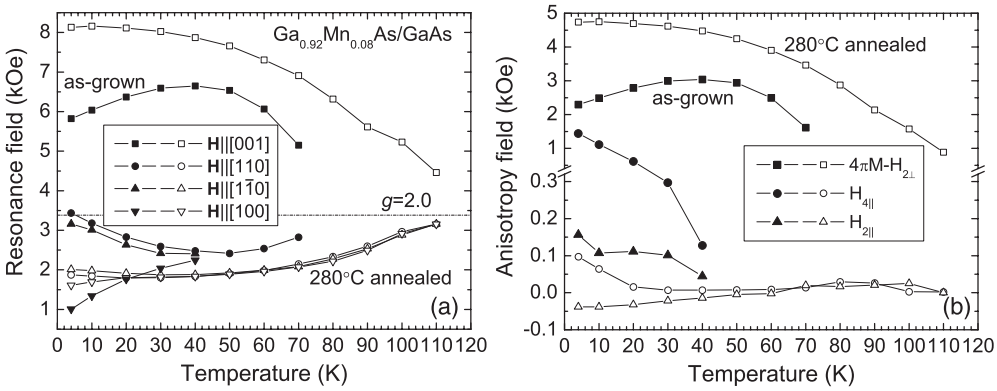

Figure 14. (a) Comparison of temperature dependences of FMR fields observed at four high symmetry field orientations for 120 nm $Ga_{0.92}Mn_{0.08}As$/GaAs before and after annealing (solid and open symbols, respectively). (b) Comparison of the anisotropy fields before and after annealing for the same sample.

evidenced by the angular variation of FMR observed when the orientation of **H** is varied in the basal (001) plane.

4.2. FMR measurements on annealed $Ga_{1-x}Mn_xAs$

It is well established that point defects such as As antisites (As_{Ga}) and Mn interstitials (Mn_I) play a crucial role in determining the magnetic properties of $Ga_{1-x}Mn_xAs$ [100]. Appropriate low temperature annealing can alter (improve) the ferromagnetism of $Ga_{1-x}Mn_xAs$, most notably by increasing its Curie temperature, magnetic moment, and hole concentration; by improving the homogeneity of the material; and by changing the temperature dependence of its magnetization to a more mean-field-like behaviour [101, 102].

To illustrate these effects, in figure 14 we compare the temperature dependence of FMR positions and magnetic anisotropy fields for a $Ga_{0.92}Mn_{0.08}As$(120 nm)/GaAs film obtained before and after annealing [67]. In the case illustrated, the annealing was carried out in the atmosphere of N_2 gas at the temperature of 280 °C for 1.0 h, and subsequently cooled by a rapid quench to room temperature. FMR positions for the four basic geometries (i.e. $\mathbf{H} \parallel [001]$, $\mathbf{H} \parallel [110]$, $\mathbf{H} \parallel [1\bar{1}0]$, and $\mathbf{H} \parallel [100]$) are shown in figure 14(a). For this compressively strained sample, the FMR occurs above the $g = 2.00$ resonance position when **H** is perpendicular to the film, and below that position for in-plane **H** orientations. Shifts from the dash–dotted line ($g = 2.00$) gradually decrease as one approaches T_C; but clearly the annealed sample has a much stronger shift than the as-grown sample when **H** is normal to the film, indicating a large increase of magnetic anisotropy due to annealing. The magnetic anisotropy fields, obtained using the four basic FMR geometries and assuming $H_{4\perp} = 0$ (this parameter is completely overshadowed by $H_{2\perp}$ due to the large compressive strain; see section 3.2), are plotted in figure 14(b) for the as-grown (solid symbols) and the annealed sample (open symbols). Figure 14(b) illustrates several basic features of magnetic anisotropy and its dependence on annealing. First, we note that annealing leads to a remarkable increase in the magnitude of the uniaxial anisotropy field $H_{2\perp}$. Second, figure 14(b) reveals that the anisotropy in the sample plane (both cubic and uniaxial) has been dramatically reduced by the annealing process. In particular, the in-plane cubic anisotropy field $H_{4\parallel}$ has decreased by more than an order of magnitude, from 1.5 to 0.1 kOe. Finally, the in-plane uniaxial anisotropy

$H_{2\parallel}$ is *positive* in the as-grown sample (the easy axis along [$\bar{1}$10]), but becomes much smaller (and eventually *negative*) in the annealed sample, causing the easy axis to favour the [110] orientation at low temperature. This ability of $H_{2\parallel}$ in annealed samples to change its sign as the temperature is increasing in fact corresponds to a type of spin reorientation transitions already discovered by SQUID measurements in earlier experiments [48].

It has been demonstrated and is now widely accepted that the highly mobile Mn_I defects diffuse to the free surface during the annealing process [16]. This improves the ferromagnetic properties of $Ga_{1-x}Mn_xAs$ as follows. By reducing the concentration of Mn interstitials, appropriate low temperature annealing increases the concentration of magnetically active Mn (which are otherwise cancelled by anti-ferromagnetically oriented nearest neighbour Mn_I), and it increases the concentration of the holes by reducing the compensation by the Mn_I donors. As noted above, it is also believed that annealing may further improve the sample quality by improving the homogeneity of the samples. XRD studies have also revealed that the out-of-plane lattice constant of $Ga_{1-x}Mn_xAs$ is reduced after annealing (while the in-plane lattice constant remains unaffected), thus implying a decrease in the compressive strain due to lattice mismatch [71]. The increase of $H_{2\perp}$ in the presence of this reduction of the built-in compressive strain can then only be attributed either to the improvement of the homogeneity or (more likely) to an increase of the hole concentration. One should note here that the SQUID magnetization studies by Sawicki *et al* [72, 48] performed on $Ga_{1-x}Mn_xAs$ samples annealed at various conditions appear to point to the influence of the hole concentration and temperature on the observed behaviour of the magnetic anisotropy (including the perpendicular and the in-plane anisotropy fields).

4.3. FMR observation of temperature-induced spin reorientation

It is expected on theoretical grounds that the orientation of the easy axis in a $III_{1-x}Mn_xV$ system is not fixed, and can be re-aligned by changing the sample parameters, such as the temperature, hole concentration, or strain. Sawicki *et al* [72] demonstrated by SQUID magnetization measurements that one can induce a spin reorientation from the [001] (normal to the sample plane) to the [100] (in-plane) direction by increasing the temperature of $Ga_{1-x}Mn_xAs$ films grown on GaAs(001) substrates with appropriately low values of the hole concentration p. Moreover, temperature-induced cross-over of the easy axes has been found not only in $Ga_{1-x}Mn_xAs$ [45, 72, 103], but also in other alloys, e.g. in AlGaMnAs [104] and $In_{1-x}Mn_xAs$ [105, 26]. Here we will show that FMR can be used to identify the mechanism of such spin reorientation by mapping out the magnetic anisotropy of the $Ga_{1-x}Mn_xAs$ sample. Specifically, we will show that the temperature dependence of the cubic and uniaxial anisotropy measured by FMR provides a natural explanation of the observed spin reorientation [106].

In figure 15, dc SQUID magnetization measurements carried out on a $Ga_{0.92}Mn_{0.08}$ As(100 nm)/$Ga_{0.85}In_{0.15}As$(1 μm) film show a remarkable temperature-dependent feature: at a low temperature (i.e. $T = 5$ K) the square-like hysteresis loops clearly show that the easy axis of magnetization is in the plane of the sample; in contrast, at a higher temperature (i.e. $T = 30$ K) the easy axis of magnetization is seen to be normal to the plane of the sample. FMR measurements have been performed on the same sample as that used in figure 15 to explore in detail the process by which such spin reorientation occurs [106]. In figure 16, we show the FMR fields in the sample of interest measured at different polar and azimuthal angles (geometry 1 and 3, respectively) at two temperatures. The resonance field at $\mathbf{H} \parallel [100]$ ($\theta_H = 0°$, $\varphi_H = 0°$) is the lowest at 4 K, but at 30 K the lowest FMR field shifts to the $\mathbf{H} \parallel [001]$ orientation ($\theta_H = 90°$). Since the lowest point in FMR data corresponds to the orientation of easy axis of the magnetization in this sample, the difference between figures 16(a) and (b)

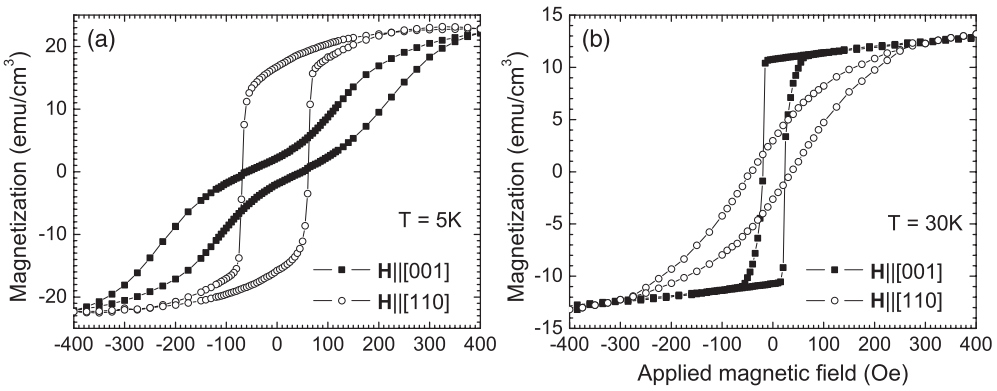

Figure 15. Magnetization as function of applied magnetic field for a $Ga_{0.92}Mn_{0.08}As(100\ nm)/Ga_{0.85}In_{0.15}As(1\ \mu m)$ film, measured by SQUID at $T = 5$ K (a) and 30 K (b). The magnetic field is applied either in the [110] or in the [001] direction. Note that the easy axis is different at the two temperatures.

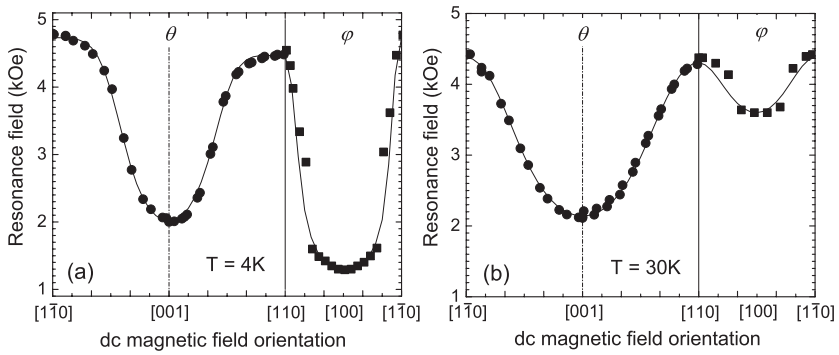

Figure 16. Angular dependences of FMR fields at 4 K (a) and 30 K (b) for a $Ga_{0.92}Mn_{0.08}As(100\ nm)/Ga_{0.85}In_{0.15}As$ (1 μm) film, each shown as three panels. The left panel corresponds to the dc magnetic field **H** and magnetization **M** in the (110) plane (geometry 1, $\varphi_H = -45°$); central is ($\bar{1}$10) plane (geometry 1, $\varphi_H = 45°$); and right is (001) plane (geometry 3, $\theta_H = 90°$). The solid curves in the figure are theoretical fits to the FMR positions H_R.

indicates that the easy axis of **M** has rotated from an in-plane direction at 4 K to normal to the plane at 30 K.

As mentioned before, the uniaxial and cubic anisotropies can be obtained from a fit to the angular-dependent data. Here we use in-plane data to determine the in-plane cubic anisotropy field ($H_{4\|}$). We then follow the fitting procedure described in section 2.4 to obtain the magnetic anisotropy fields and the g-factor ($\sim 2.0 \pm 0.1$) in the sample under investigation. Note that the procedure yields a small value of $H_{4\perp}$ due to the large built-in tensile strain in the $Ga_{1-x}Mn_xAs/Ga_{1-y}In_yAs$ layer (see section 3.2). The best-fit curves according to equations (6)–(8) are also plotted in figure 16 for comparison.

The resonance and anisotropy fields obtained from the FMR analysis are shown in figure 17 as a function of temperature. In figure 17(a) we observe a steady evolution of resonance fields at **H** $\|$ [100] as the temperature is raised from 4 to 30 K, indicating a continuous anisotropy change and the accompanying spin rotation. In figure 17(b) the temperature dependences of $4\pi M_{eff}$ and $H_{4\|}$ are especially informative, and we believe that their behaviour plays a

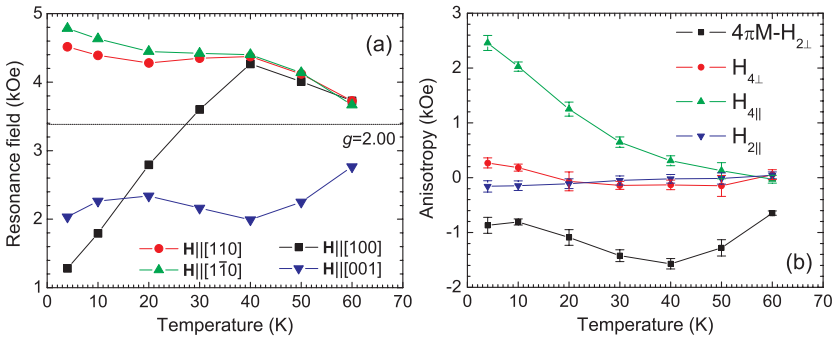

Figure 17. (a) Temperature dependence of the FMR fields at four basic orientations of **H** for a $Ga_{0.92}Mn_{0.08}As(100\ nm)/Ga_{0.85}In_{0.15}As$ (1 μm) film. (b) Temperature dependence of the anisotropy fields $4\pi M - H_{2\perp}$, $H_{4\|}$, $H_{4\perp}$, and $H_{2\|}$ obtained from the FMR data in panel (a).

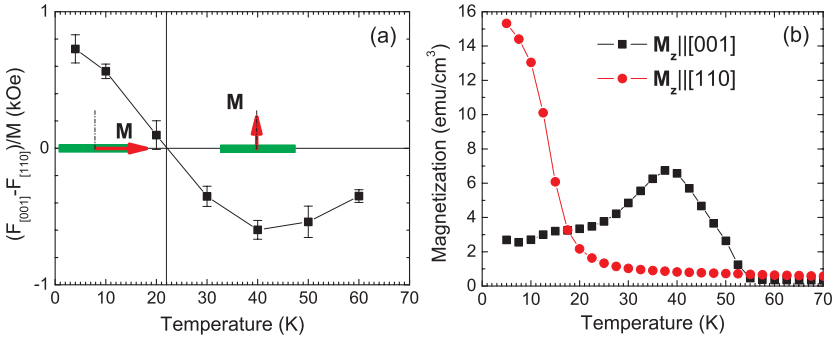

Figure 18. (a) Temperature dependence of the free energy difference between **M** ∥ [001] and **M** ∥ [110] for a $Ga_{0.92}Mn_{0.08}As(100\ nm)/Ga_{0.85}In_{0.15}As(1\ \mu m)$ film using the anisotropy parameters plotted in (b). (b) Remanent magnetization as function of temperature T observed by SQUID for two crystalline axes. Note that a spin reorientation transition occurs at $T \sim 20$ K.

crucial role in the process of the easy axis reorientation. At the lowest temperatures the magnitude of the cubic anisotropy is much larger than that of the perpendicular uniaxial anisotropy. This causes the magnetic moments of Mn^{2+} ions to align themselves in the plane. However, the cubic anisotropy term varies rapidly with temperature, quickly diminishing as the temperature increases. As a result, above 20 K the perpendicular uniaxial anisotropy becomes dominant, causing the spins to rotate to a new easy axis perpendicular to the sample surface. The cause of this spin reorientation is clarified in figure 18. In figure 18(a) the difference between the free energy when **M** ∥ [001] and **M** ∥ [110] calculated with the parameters obtained from FMR is shown as function of temperature for the sample of interest, and the remanent magnetizations measured by SQUID for the [110] and [001] directions are plotted in figure 18(b) for comparison. Thus the behaviour of the free energy shown in figure 18 clearly suggests that the spin reorientation in the studied samples can be fully understood in terms of the competition between the uniaxial and the cubic anisotropy.

Changes of **M** as a function of temperature have been studied in several $III_{1-x}Mn_xV$ systems experimentally (see, e.g., [104, 26, 72, 48, 103]) as well as theoretically (see, e.g., [30]). Note that the magnetic anisotropy in $III_{1-x}Mn_xV$ systems corresponds to the symmetry of the hole subbands as shaped by the strain, and the geometry and the population of these sub-bands depend on the magnetization (through Zeeman splitting) and on the hole

concentration, both of which are functions of temperature. It is therefore important to explore the temperature dependence of anisotropy with the aim to fully understand the mechanism of ferromagnetism in $III_{1-x}Mn_xV$ systems. While the physical origins of the dependence of magnetic anisotropy on temperature are complicated and as yet unclear, it is important to appreciate that such dependence provides an important practical opportunity for manipulation of magnetic anisotropy (e.g. through the bolometric effect [26]), which is in turn likely to lead to future device applications. It is therefore especially important to address this issue by further rigorous theoretical studies.

5. FMR linewidth and relaxation of magnetization

5.1. Angular and temperature dependences of FMR linewidth

The peak-to-peak ferromagnetic resonance linewidth ΔH_{pp} is a measure of the relaxation rate of the magnetization. ΔH_{pp} is caused by two mechanisms: intrinsic relaxation of magnetization (often referred to as Gilbert damping); and relaxation caused by magnetic inhomogeneities within the ferromagnet. Although these mechanisms are far from understood in $III_{1-x}Mn_xV$ alloys, for completeness in this section we will present the observed behaviour of the FMR linewidth ΔH_{pp} as a function of temperature and field orientation for a representative $Ga_{1-x}Mn_xAs$ sample. In general, the linewidth can be expressed as follows [107, 42]:

$$\Delta H_{pp} = \Delta H_{inhom} + \Delta H_{hom} = \Delta H_{inhom} + \frac{2}{\sqrt{3}}\frac{G}{\gamma^2 M}\omega. \tag{10}$$

Here the second term—the Gilbert damping—reflects 'viscous' damping of the precessive motion of magnetization associated with FMR, and is frequency dependent, as seen in equation (10). The first term on the right in equation (10)—the inhomogeneous broadening ΔH_{inhom}—is caused by sample imperfections, and can be viewed as arising from a distribution of resonance fields that vary slightly from point to point, thus increasing the width of the FMR absorption as a whole. Such imperfection may include local fluctuations of alloy composition and fluctuations of hole concentration, as well as variations from point to point in the orientation of magnetic anisotropy. As a result, this part of the FMR linewidth provides a measure of the homogeneity of a magnetic sample. Note that the narrowest lines are usually observed for samples which are structurally and magnetically most homogeneous. However, by considering the coupling between the uniform mode resonance ($k = 0$) and the spin waves ($k \neq 0$) [108], one must realize that the narrowest line may not necessarily correspond to the field applied along either the easy axis or the hard axis.

Like the FMR field position, ΔH_{pp} shows a distinct dependence on the orientation of the magnetic field with respect to the crystal axes of the specimen [109]. This is clearly seen in figure 19(a), which shows the FMR linewidth for a 300 nm thick $Ga_{0.97}Mn_{0.03}As$/GaAs sample when **H** is in the sample plane (geometry 3; left panel), and when **H** is rotated from the in-plane ([110]) to the out-of-plane ([001]) (geometry 1; right panel). Very similar angular behaviour of the linewidth is observed in other $Ga_{1-x}Mn_xAs$/GaAs samples. It is rather striking that the FMR linewidth becomes very narrow for $\mathbf{H} \parallel [100]$ (about 100 Oe), and broadens by a factor of three when the field is rotated by 90° in either direction in geometry 3 (i.e. when the field is confined to the plane of the film). Note that the strong dependence of the FMR linewidth on the field orientation suggests that magnetic inhomogeneities in the ferromagnetic layer contribute significantly to the FMR broadening [107, 110]. According to equation (8), a large inhomogeneity of the anisotropy parameter—$\Delta H_{4\parallel}$ in the case of geometry 3—would produce such a large angular-dependent FMR linewidth. However, the analysis of ΔH_{pp} becomes more complicated by the fact that the shape of the resonance line will differ from a pure Gaussian or

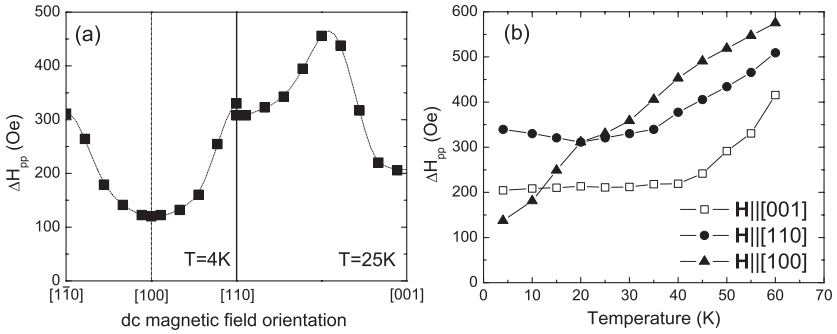

Figure 19. (a) Angular dependence of the FMR peak to peak linewidth ΔH_{pp} for $Ga_{0.97}Mn_{0.03}As/GaAs$ observed in geometry 3 (left panel) and geometry 1 (right panel)—as a function of the azimuthal angle φ_H and the polar angle θ_H, respectively. The lines are guides for the eye. (b) Temperature dependence of ΔH_{pp} observed in three high symmetry field configurations: **H** ∥ [001], **H** ∥ [110], and **H** ∥ [100].

Lorentzian if the resonance field is applied at intermediate angles between an easy and a hard magnetic axis. In this case the orientation of **M** would be expected to vary with the applied field strength, and differences in the degree of 'dragging' of the magnetization by the field would in turn cause changes in FMR for different points within the specimen, thus broadening the resonance line [111]—yet another manifestation of inhomogeneous broadening.

As shown in figure 19(b), ΔH_{pp} is consistently seen to broaden as the temperature is increased for the same sample. Again the behaviour of the temperature dependence of ΔH_{pp} is similar to that observed in other $Ga_{1-x}Mn_xAs/GaAs$ samples. Note that the respective linewidths for **H** ∥ [001] and **H** ∥ [110] remain relatively constant to approximately 40 K (i.e. over the major range of temperatures where $Ga_{1-x}Mn_xAs$ is ferromagnetic), but begin to broaden rapidly as one approaches the Curie temperature T_C. This can be understood as an increase of scattering ('de-phasing') due to spin disorder, which is expected to increase rapidly as one comes close to the ferromagnetic-to-paramagnetic transition and the long range coherence becomes disrupted. In other words, as the long range FM mode vanishes at T_C, the contribution of intrinsic damping to ΔH_{pp} (seen in equation (10)) increases accordingly. In light of the remarks just made, we find the behaviour of ΔH_{pp} observed for **H** ∥ [100] to be quite anomalous: the linewidth in this orientation is the narrowest at low temperatures; and it broadens steadily to become the widest at high temperatures. We tentatively attribute this to a re-orientation of the easy axis (see section 4.3) as the temperature increases [45].

5.2. *Effect of annealing on the FMR linewidth*

Finally, we wish to point to the dramatic narrowing of the FMR linewidth observed after $Ga_{1-x}Mn_xAs$ has been annealed, as shown in figure 20 [112]. In figure 20(a) the angular dependence of the FMR linewidth is shown for both as-grown and annealed $Ga_{0.92}Mn_{0.08}As$(120 nm)/GaAs samples investigated in [67] and [112], when the dc magnetic field **H** is confined to the sample plane (left panel), and when it is rotated from the in-plane [110] orientation to the [001] direction normal to the layer (right panel). When **H** is in the plane (left panel), the as-grown sample has larger and more divergent linewidths at all angles, but otherwise the angular dependence of ΔH_{pp} is very similar for both as-grown and annealed samples—the FMR linewidth is the narrowest when the field is applied along the easy axis, **H** ∥ [100], but wider for **H** ∥ [110] and [1$\bar{1}$0]. On the other hand, when H is rotated from the

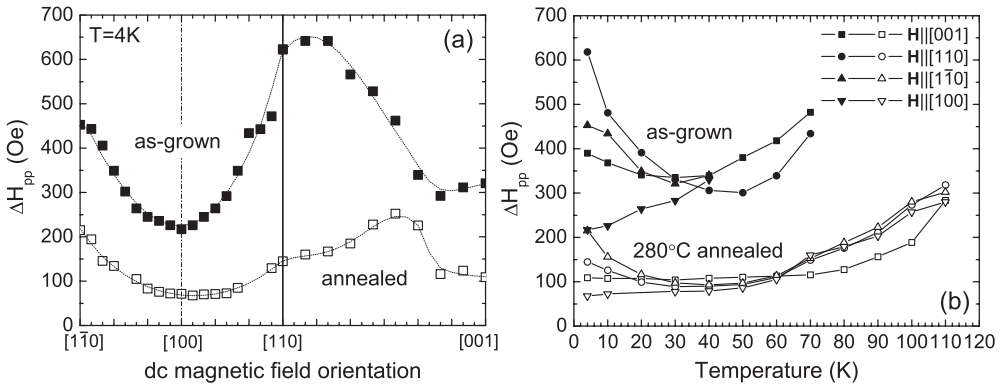

Figure 20. Experimental FMR peak-to-peak linewidth ΔH_{pp} in as-grown (solid symbols) and annealed (open symbols) $Ga_{0.92}Mn_{0.08}As$ measured (a) at 4 K as a function of the azimuthal and polar angles of the applied field and (b) as a function of temperature for four high symmetry dc magnetic-field orientations indicated in the figure. The curves in (a) are guides for the eye.

in-plane (**H** ∥ [110]) to the out-of-plane (**H** ∥ [001]) orientation as shown in the right panel, the FMR linewidth becomes not only narrower after annealing, but also the angular dependence of the linewidth changes quite drastically. The intuitive interpretation of this behaviour is that the magnetic properties of as-grown samples are much more inhomogeneous than those in annealed specimens [113]. Note that the narrowest lines are found as one approaches the hard axis (i.e. the [001] direction) or the easy axis (i.e. the [100] direction) for both as-grown and annealed samples.

The temperature dependences of ΔH_{pp} for both as-grown and annealed samples are shown in figure 20(b) for the four basic geometries (i.e. **H** ∥ [001], **H** ∥ [110], **H** ∥ [1$\bar{1}$0], and **H** ∥ [100]). It is clear that the variation of the linewidth with angle becomes strikingly weaker after annealing, especially at low temperatures. Furthermore, the resonance linewidth of the annealed samples becomes narrower by almost one-third compared to the case of as-grown specimens, as seen in both panels of figure 20. This observation is consistent with the improved quality of the sample (as indicated, e.g., by the enhanced T_C, and especially by the more Brillouin-like temperature dependence of the magnetization), and also by the increase of the size of magnetically homogeneous regions [73]. Since it has already been established that annealing reduces the number of Mn interstitials [100]—and since it is reasonable to expect (and in fact experimentally confirmed) that the annealing process also serves to 'smooth out' local inhomogeneities [113]—we are tempted to suggest that the spectacular narrowing of FMR evident in annealed specimens is in some way related to the reduction of inhomogeneous broadening associated with the removal of local defects by such post-growth heat treatment. As a result, the experimental results in figure 20 imply that the leading contribution to the FMR linewidth in annealed samples might come predominantly from the homogeneous (Gilbert damping) broadening [112].

5.3. The Gilbert damping coefficient

From the macroscopic point of view, the intrinsic (i.e., Gilbert) damping term reflects the 'viscous' damping of the motion of magnetization associated with FMR, as described on the right side of equation (2). Thus the Gilbert coefficient G in equations (2) and (10) is one of the key parameters that characterize collective magnetization dynamics in a ferromagnet.

Early theories of magnetization dynamics in transition metals viewed exchange coupling ($\propto \mathbf{S}\cdot\mathbf{s}$) between the localized d-shell spins $\mathbf{S}$ and the itinerant s–p band carrier spins $\mathbf{s}$ as a key relaxation mechanism [114]. It was later found that this microscopic view needs to be modified for transition metals to account for the itinerant character of their d-electrons. On the other hand, in many FMSs (e.g. $Ga_{1-x}Mn_xAs$), models of localized d-shell moments that are exchange-coupled to itinerant s–p band carriers—in this case itinerant holes—provide a good description of their ferromagnetism [8]. Thus the p–d exchange-coupling between localized moments and itinerant holes should also contribute significantly to Gilbert damping in ferromagnetic semiconductor systems such as $Ga_{1-x}Mn_xAs$. The basic process for this damping mechanism can be viewed as comprised of two steps: first, a local-moment magnon (spin wave) is annihilated by p–d exchange interaction with a hole that suffers a spin flip; second, the spin of the itinerant hole then relaxes through spin–orbit interaction [112]. As a result, the Gilbert damping of the precession of magnetization discussed here is intimately dependent on the spin–orbit characteristic of the valence band.

A fully microscopic theory of the kinetic-exchange contribution to the Gilbert coefficient in DMSs is presented by Sinova *et al* [112]. By comparing the linear response predicted by the classical phenomenological Landau–Lifshitz–Gilbert (LLG) equation with microscopic linear-response theory, the authors of [112] identify the Gilbert coefficient with the dissipative part of the susceptibility diagram. Furthermore, this mechanism implies that the theoretical Gilbert damping coefficient strongly depends on Mn-moment density, hole concentration, and lifetime of the hole spin (the value of lifetime was chosen to be in the range estimated in previous detailed studies of transport properties of these systems [115]). Note that comparison of the theoretically calculated Gilbert coefficient with experimental FMR data presented above suggests that in annealed strongly metallic samples the p–d coupling contributes significantly to the damping rate of the magnetization precession at low temperatures. However, since the frequency dependence of the FMR linewidth is not available, it is not possible at this time to experimentally decouple the inhomogeneous broadening from the intrinsic Gilbert damping contributions to the FMR linewidth, and to make a quantitative comparison with the theory.

Gilbert damping depends intrinsically on the spin–orbit interaction, which is in turn related to the finite spin lifetime of the valence band holes. According to the analysis of Kambersky [116] of scattering processes of itinerant electron spins and phonons, one can then assume that G is related to the g-factor of the Mn-ion/hole complex,

$$G \propto (g-2)^2. \tag{11}$$

As a result, considering the dependence of the g-factor on the hole concentration p as discussed in section 3.2, equation (11) implies that G will increase with increasing p, which is consistent with the theoretical calculations in [112]. Such consistency thus reflects the validity of the picture of the Mn-ion/hole complex—which is formed by strong p–d exchange-coupling between the localized Mn moments and the itinerant holes—precessing in unison in the local static field in FMR measurement, as has already been argued in connection with the effective g-factor. It is clear from the above discussion that extending the measurements of the FMR linewidth to other frequencies would contribute to a better understanding of the Gilbert damping coefficient in $Ga_{1-x}Mn_xAs$ and other $III_{1-x}Mn_xV$ alloys.

6. Concluding remarks

In reviewing the experimental and theoretical material presented above it was our hope to demonstrate that FMR is a powerful—and at the same time a versatile—tool for investigating magnetic properties of ferromagnetic semiconductor alloys and their heterostructures. In the

presentation we have used FMR results obtained on $Ga_{1-x}Mn_xAs$, since most FMR studies so far were carried out on this material; but all conclusions presented are expected to apply equally well to other $III_{1-x}Mn_xV$ systems.

The unambiguous observation of FMR in $Ga_{1-x}Mn_xAs$ constitutes, of course, yet another convincing demonstration of ferromagnetism in this material. In this context the appearance of clear spin wave resonances is especially valuable, in that they represent an interference of coherent magnetic excitations spanning the entire sample, thus attesting to the long range character of ferromagnetic ordering across the entire sample.

In terms of serving as an experimental tool, FMR experiments—and particularly experiments performed as a function of angle between the applied magnetic field and crystallographic axes of the specimen—have proved invaluable in providing a rather complete understanding of magnetic anisotropy parameters characterizing $Ga_{1-x}Mn_xAs$. This aspect of FMR arises from the fact that the angular symmetry of FMR directly reflects the symmetry of free energy, which for any given function depends very directly on the numerical values of the cubic ($K_{4\perp}$ and $K_{4\parallel}$) and uniaxial ($K_{2\perp}$ and $K_{2\parallel}$) anisotropy terms. Thus, carrying out FMR measurements on strategically selected series of samples enabled the investigators to identify how the various anisotropy terms depend on strain, temperature, annealing, and doping. This capability of FMR has a practical relevance to the field of spintronics, since understanding and controlling magnetic anisotropy parameters are essential for the design of devices based on spin polarization in the new $III_{1-x}Mn_xV$ alloys and their multilayers.

On the fundamental level, the correlation of the behaviour of magnetic anisotropy obtained from FMR with the properties of the valence band (hole concentration, doping, and other aspects that affect the Fermi energy) is particularly informative, since it is the properties of the holes (i.e. the anisotropy of the hole Fermi surface) that ultimately determine magneto-crystalline anisotropy of $Ga_{1-x}Mn_xAs$. Indeed, the dependences of the various magnetic anisotropy ($K_{4\perp}$, $K_{4\parallel}$, and $K_{2\perp}$) on strain conditions, temperature, and doping levels are a direct reflection of how these external parameters affect the behaviour of the (heavy and light) holes at the Fermi level. A conspicuous exception to this relationship of the various values of K_i with the Fermi surface of the holes within $Ga_{1-x}Mn_xAs$ is the emergence of a finite value of $K_{2\parallel}$ representing *uniaxial* anisotropy in the fourfold symmetric (001) plane. While some suggestions of this anisotropy have been made, it must be stated that its origin remains unresolved, and may be related to mechanisms other than the nature of hole-mediated exchange between the Mn^{2+} ions.

Continuing with the issues involving the role of holes in the FMR phenomenon, it must be strongly emphasized that FMR represents a *collective* precession of the system of Mn^{2+} magnetic moments and the valence band holes that act in unison, coupled by exchange interaction. The ability of determining the effective g-factor for such *collective* precession thus provides the opportunity to measure the contribution of the holes themselves to the magnetization of the system as a whole. While at this time we only have first experimental indications of such a contribution of the holes to $\mathbf{M}$ (as evidenced by the unambiguous reduction of the g-factor below the value of 2.00, the reduction increasing with increasing hole concentration), this result clearly points to the opportunity provided by FMR for exploring this contribution in detail in future experiments. This we feel is quite important, because the various factors determining the total $\mathbf{M}$ of the system are difficult (if not impossible) to separate in dc magnetization measurements.

While a great deal is now understood about the FMR position in $Ga_{1-x}Mn_xAs$ (as can be judged from the rather excellent theoretical fits to the resonance field as a function of angle), the study on peak-to-peak FMR linewidth still remains relatively unexplored. We feel strongly that this direction should be vigorously pursued, inasmuch as the information

of magnetization lifetime is a key parameter for all processes relying on spin coherence in $Ga_{1-x}Mn_xAs$ and related $III_{1-x}Mn_xV$ alloys. The problem here is of course complicated by the presence of two different mechanisms that contribute to FMR broadening: the intrinsic Gilbert damping term G, and the effect of inhomogeneities. Although separating these contributions is difficult, we have already seen that, in the FMR, linewidth can be dramatically affected by such processes as annealing. These latter very striking results suggest that linewidth experiments on samples with strategically planned properties (such as the hole concentration and various attempts at reducing inhomogeneities) may lead us to a better understanding of how to control magnetization lifetime in $III_{1-x}Mn_xV$ alloys.

While the work on FMR in $Ga_{1-x}Mn_xAs$ reviewed in this review clearly establishes it as a powerful tool for the study of many of its magnetic properties (some of which are difficult to determine by other methods), several aspects of FMR in the $III_{1-x}Mn_xVs$ are still poorly understood. The most notable among these is the origin of the in-plane magnetic anisotropy (also observed in more standard measurements, such as SQUID); and the entire issue of magnetization relaxation. Nevertheless our understanding of FMR is now sufficiently complete to undertake FMR studies of systems other than simple $III_{1-x}Mn_xV$ epilayers grown on the (001) plane, which constituted the main focus of this review. In particular, FMR studies of epilayers grown on high index planes or on vicinal (tilted) substrates should shed additional valuable light on magneto-crystalline symmetry issues that characterize these materials. FMR studies on exchange-biased $III_{1-x}Mn_xV$ layers should further extend our understanding of the symmetry of the ferromagnetic structure in these materials to unidirectional anisotropy—an issue that is of interest both for understanding exchange coupling across antiferromagnetic/ferromagnetic interfaces and—on a practical level—for design of $III_{1-x}Mn_xV$-based devices. Finally, FMR studies of $III_{1-x}Mn_xV$-based multilayers should also shed valuable light on the coupling between ferromagnetic layers across non-magnetic 'spacers'. All these options still await exploration, but the excellent correlation between experiment and theory described in this review indicate that FMR can be extremely useful in the study of these more advanced structures.

Acknowledgments

We would like to thank our numerous co-workers and co-authors (see references) for their stimulating and fruitful discussions, and their very significant contributions to many aspects of FMR reviewed in this article. This work was supported in part by NSF grants DMR02-10519 and DMR02-45227.

References

[1] Prinz G A 1990 *Science* **250** 1092
[2] Wolf S A, Awschalom D D, Buhrman R A, Daughton J M, von Molnár S, Roukes M L, Chtchelkanova A Y and Treger D M 2001 *Science* **294** 1488
[3] Furdyna J K and Kossut J (ed) 1988 *Semiconductors and Semimetals* vol 25 (New York: Academic)
[4] Furdyna J K 1988 *J. Appl. Phys.* **64** R29
[5] Haury A, Wasiela A, Arnoult A, Cibert J, Tatarenko S, Dietl T and d'Aubigné Y M 1997 *Phys. Rev. Lett.* **79** 511
[6] Ohno H 1998 *Science* **281** 951
[7] Furdyna J K, Schiffer P, Sasaki Y, Potashnik S J and Liu X Y 2000 *Optical Properties of Semiconductor Nanostructures* (*NATO Science Series* vol 81) ed M L Sadowski, M Potemski and M Grynberg (Dordrecht: Kluwer) pp 211–24
[8] Ohno H 1999 *J. Magn. Magn. Mater.* **200** 110
[9] Furdyna J K, Liu X, Lim W L, Sasaki Y, Wojtowicz T, Kuryliszyn I, Lee S, Yu K M and Walukiewicz W 2003 *J. Korean Phys. Soc.* **42** S579

[10] MacDonald A H, Schiffer P and Samarth N 2005 *Nat. Mater.* **4** 195
[11] Munekata H, Ohno H, von Molnár S, Segmüller A, Chang L L and Esaki L 1989 *Phys. Rev. Lett.* **63** 1849
[12] Ohno H, Munekata H, Penney T, von Molnár S and Chang L L 1992 *Phys. Rev. Lett.* **68** 2664
[13] De Boeck J, Oesterholt R, Van Esch A, Bender H, Bruynseraede C, Van Hoof C and Borghs G 1996 *Appl. Phys. Lett.* **68** 2744
[14] Ohno H, Shen A, Matsukura F, Oiwa A, Endo A, Katsumoto S and Iye Y 1996 *Appl. Phys. Lett.* **69** 363
[15] Ku K C *et al* 2003 *Appl. Phys. Lett.* **82** 2302
[16] Edmonds K W *et al* 2004 *Phys. Rev. Lett.* **92** 037201
[17] Adell M, Ilver L, Kanski J, Stanciu V, Svedlindh P, Sadowski J, Domagala J Z, Terki F, Hernandez C and Charar S 2005 *Appl. Phys. Lett.* **86** 112501
[18] Wang K Y, Campion R P, Edmonds K W, Sawicki M, Dietl T, Foxon C T and Gallagher B L 2005 *AIP Conf. Proc.* **772** 333
[19] Matsukura F, Abe E and Ohno H 2000 *J. Appl. Phys.* **87** 6442
[20] Lim W L, Wojtowicz T, Liu X, Dobrowolska M and Furdyna J K 2004 *Physica* E **20** 346
[21] Wojtowicz T *et al* 2003 *Appl. Phys. Lett.* **82** 4310
[22] Zutic I, Fabian J and Das Sarma S 2004 *Rev. Mod. Phys.* **76** 323
[23] Ohno Y, Young D K, Beschoten B, Matsukura F, Ohno H and Awschalom D D 1999 *Nature* **402** 790
[24] Ohno H, Chiba D, Matsukura F, Omiya T, Abe E, Dietl T, Ohno Y and Ohtani K 2000 *Nature* **408** 944
[25] Koshihara S, Oiwa A, Hirasawa M, Katsumoto S, Iye Y, Urano C, Takagi H and Munekata H 1997 *Phys. Rev. Lett.* **78** 4617
[26] Liu X *et al* 2004 *Physica* E **20** 370
[27] Goennenwein S T B, Wassner T A, Huebl H, Brandt M S, Philipp J B, Opel M, Gross R, Koeder A, Schoch W and Waag A 2004 *Phys. Rev. Lett.* **92** 227202
[28] Akai H 1998 *Phys. Rev. Lett.* **81** 3002
[29] König J, Lin H-H and MacDonald A H 2000 *Phys. Rev. Lett.* **84** 5628
[30] Dietl T, Ohno H and Matsukura F 2001 *Phys. Rev.* B **63** 195205
[31] Litvinov V I and Dugaev V K 2001 *Phys. Rev. Lett.* **86** 5593
[32] Inoue J, Nonoyama S and Itoh H 2000 *Phys. Rev. Lett.* **85** 4610
[33] Sanvito S, Ordejón P and Hill N A 2001 *Phys. Rev.* B **63** 165206
[34] Timm C, Schäfer F and von Oppen F 2002 *Phys. Rev. Lett.* **89** 137201
[35] Das Sarma S, Hwang E H and Kaminski A 2003 *Phys. Rev.* B **67** 155201
[36] Dietl T, Ohno H, Matsukura F, Cibert J and Ferrand D 2000 *Science* **287** 1019
[37] Schmidt G and Molenkamp L 2002 *Semiconductor Spintronics and Quantum Computing* ed A D Awschalom, D Loss and N Samarth (Berlin: Springer)
[38] Chiba D, Akiba N, Matsukura F, Ohno Y and Ohno H 2000 *Appl. Phys. Lett.* **77** 1873
Tanaka M and Higo Y 2001 *Phys. Rev. Lett.* **87** 026602
Chun S H, Potashnik S J, Ku K C, Schiffer P and Samarth N 2002 *Phys. Rev.* B **66** 100408
[39] Tang H X, Kawakami R K, Awschalom D D and Roukes M L 2003 *Phys. Rev. Lett.* **90** 107201
[40] Rüster C, Borzenko T, Gould C, Schmidt G, Molenkamp L W, Liu X, Wojtowicz T J, Furdyna J K, Yu Z G and Flatté M E 2003 *Phys. Rev. Lett.* **91** 216602
[41] Abolfath M, Jungwirth T, Brum J and MacDonald A H 2001 *Phys. Rev.* B **63** 054418
[42] Farle M 1998 *Rep. Prog. Phys.* **61** 755
[43] Poole C P 1967 *Electron Spin Resonance* (New York: Interscience)
[44] Welp U, Vlasko-Vlasov V K, Menzel A, You H D, Liu X, Furdyna J K and Wojtowicz T 2004 *Appl. Phys. Lett.* **85** 260
[45] Welp U, Vlasko-Vlasov V K, Liu X, Furdyna J K and Wojtowicz T 2003 *Phys. Rev. Lett.* **90** 167206
[46] Moore G P, Ferré J, Mougin A, Moreno M and Däweritz L 2003 *J. Appl. Phys.* **94** 4530
[47] Hamaya K, Taniyama T, Kitamoto Y, Moriya R and Munekata H 2003 *J. Appl. Phys.* **94** 7657
[48] Sawicki M *et al* 2005 *Phys. Rev.* B **71** 121302(R)
[49] Griffiths J H E 1946 *Nature* **158** 670
[50] Kittel C 1947 *Phys. Rev.* **71** 270
[51] Holm R T and Furdyna J K 1974 *Solid State Commun.* **15** 1459
[52] Holm R T and Furdyna J K 1977 *Phys. Rev.* B **15** 844
[53] Mullin D P, Galazka R R and Furdyna J K 1981 *Phys. Rev.* B **24** 355
[54] Oseroff S B 1982 *Phys. Rev.* B **25** 6584
[55] Kremer R E and Furdyna J K 1983 *J. Magn. Magn. Mater.* **40** 185
[56] Kremer R E and Furdyna J K 1985 *Phys. Rev.* B **31** 1
[57] Kremer R E and Furdyna J K 1988 *Phys. Rev.* B **37** 4875

[58] Samarth N and Furdyna J K 1988 *Phys. Rev.* B **37** 9227
[59] Title R S 1969 *J. Appl. Phys.* **40** 4902
[60] Schneider J, Kaufmann U, Wilkening W, Baeumler M and Köhl F 1987 *Phys. Rev. Lett.* **59** 240
[61] Twardowski A 1999 *Mater. Sci. Eng.* B **63** 96
[62] Szczytko J, Twardowski A, Palczewska M, Jablonski R, Furdyna J and Munekata H 2001 *Phys. Rev.* B **63** 085315
[63] Nojiri H, Motokawa M, Takeyama S, Matsukura F and Ohno H 1998 *Physica* B **256–258** 569
[64] Sasaki Y, Liu X, Furdyna J K, Palczewska M, Szczytko J and Twardowski A 2002 *J. Appl. Phys.* **91** 7484
[65] Goennenwein S T B, Graf T, Wassner T, Brandt M S, Stutzmann M, Koeder A, Frank S, Schoch W and Waag A 2003 *J. Supercond.* **16** 75
[66] Balascuta S, Carini1 J, Chipara M, Liu X, Wojtowicz T, Sasaki Y and Furdyna J K, unpublished
[67] Liu X, Sasaki Y and Furdyna J K 2003 *Phys. Rev.* B **67** 205204
[68] Dziatkowski K, Palczewska M, Słupiński T and Twardowski A 2004 *Phys. Rev.* B **70** 115202
[69] Liu X, Lim W L, Ge Z, Shen S, Dobrowolska M, Furdyna J K, Wojtowicz T, Yu K M and Walukiewicz W 2005 *Appl. Phys. Lett.* **86** 112512
[70] Stoner E C and Wohlfarth E P 1948 *Phil. Trans. R. Soc.* A **240** 599
[71] Kuryliszyn-Kudelska I, Domagała J Z, Wojtowicz T, Liu X, Lusakowska E, Dobrowolski W and Furdyna J K 2004 *J. Appl. Phys.* **95** 603
[72] Sawicki M, Matsukura F, Idziaszek A, Dietl T, Schott G M, Ruester C, Gould C, Karczewski G, Schmidt G and Molenkamp L W 2004 *Phys. Rev.* B **70** 245325
[73] Hamaya K, Taniyama T, Kitamoto Y, Fujii T and Yamazaki Y 2005 *Phys. Rev. Lett.* **94** 147203
[74] Wigen P E 1964 *Phys. Rev.* **133** A1557
[75] Aspelmeier A, Tischer M, Farle M, Russo M, Baberschke K and Arvanitis D 1995 *J. Magn. Magn. Mater.* **146** 256
[76] Heinrich B 1994 *Ultrathin Magnetic Structures* vol I/II (Berlin: Springer)
[77] Suhl H 1955 *Phys. Rev.* **97** 555
[78] Maksymowicz A Z and Leaver K D 1973 *J. Phys. F: Met. Phys.* **3** 1031
[79] Liu X, Lim W L, Titova L V, Dobrowolska M, Furdyna J K, Kutrowski M and Wojtowicz T 2005 *J. Appl. Phys.* **98** 63904
[80] Liu X, Lim W L, Dobrowolska M, Furdyna J K and Wojtowicz T 2005 *Phys. Rev.* B **71** 035307
[81] Cochran J F 1994 *Ultrathin Magnetic Structures* vol I/II (Berlin: Springer)
[82] Sasaki Y, Liu X and Furdyna J K 2003 *J. Supercond.* **16** 41
[83] Goennenwein S T B *et al* 2003 *Appl. Phys. Lett.* **82** 730
[84] Kittel C 1958 *Phys. Rev.* **110** 1295
[85] Rappoport T G, Redliński P, Liu X, Zaránd G, Furdyna J K and Jankó B 2004 *Phys. Rev.* B **69** 125213
[86] Mitsumori Y, Oiwa A, Słupiński T, Maruki H, Kashimura Y, Minami F and Munekata H 2004 *Phys. Rev.* B **69** 033203
[87] Chung S J, Lee S, Park I W, Liu X and Furdyna J K 2004 *J. Appl. Phys.* **95** 7402
[88] Tang H X, Masmanidis S, Kawakami R K, Awschalom D D and Roukes M L 2004 *Nature* **431** 52
[89] Sawicki M, Matsukura E, Dietl T, Schott G M, Ruester C, Schmidt G, Molenkamp L W and Karczewski G 2003 *J. Supercond.* **16** 7
[90] Wojtowicz T, Lim W L, Liu X, Dobrowolska M, Furdyna J K, Yu K M, Walukiewicz W, Vurgaftman I and Meyer J R 2003 *Appl. Phys. Lett.* **83** 4220
[91] Yu K M, Walukiewicz W, Wojtowicz T, Lim W L, Liu X, Dobrowolska M and Furdyna J K 2004 *Appl. Phys. Lett.* **84** 4325
[92] Lax B and Button K J 1962 *Microwave Ferrites and Ferrimagnetics* (New York: McGraw-Hill)
Wangsness R K 1953 *Phys. Rev.* **91** 1085
[93] Rubinstein M, Hanbicki A, Lubitz P, Osofsky M, Krebs J J and Jonker B 2002 *J. Magn. Magn. Mater.* **250** 164
[94] Szczytko J, Mac W, Stachow A, Twardowski A, Becla P and Tworzydło J 1996 *Solid State Commun.* **99** 927
[95] Hartmann T, Lampalzer M, Stolz W, Megges K, Lorberth J, Klar P J and Heimbrodt W 2000 *Thin Solid Films* **364** 209
[96] Okabayashi J, Kimura A, Rader O, Mizokawa T, Fujimori A, Hayashi T and Tanaka M 1998 *Phys. Rev.* B **58** 4211(R)
[97] Szczytko J, Bardyszewski W and Twardowski A 2001 *Phys. Rev.* B **64** 075306
[98] Schliemann J, König J and MacDonald A H 2001 *Phys. Rev.* B **64** 165201
[99] Potashnik S J, Ku K C, Mahendiran R, Chun S H, Wang R F, Samarth N and Schiffer P 2002 *Phys. Rev.* B **66** 012408
Potashnik S J, Ku K C, Wang R F, Stone M B, Samarth N, Schiffer P and Chun S H 2003 *J. Appl. Phys.* **93** 6784

[100] Yu K M, Walukiewicz W, Wojtowicz T, Kuryliszyn I, Liu X, Sasaki Y and Furdyna J K 2002 *Phys. Rev.* B **65** 201303(R)
[101] Hayashi T, Hashimoto Y, Katsumoto S and Iye Y 2001 *Appl. Phys. Lett.* **78** 1691
[102] Potashnik S J, Ku K C, Chun S H, Berry J J, Samarth N and Schiffer P 2001 *Appl. Phys. Lett.* **79** 1495
[103] Wang K-Y, Sawicki M, Edmonds K W, Campion R P, Maat S, Foxon C T, Gallagher B L and Dietl T 2005 *Phys. Rev. Lett.* **95** 217204
[104] Takamura K, Matsukura F, Chiba D and Ohno H 2002 *Appl. Phys. Lett.* **81** 2590
[105] Endo T, Słupiński T, Yanagi S, Oiwa A and Munekata H, unpublished
[106] Liu X and Furdyna J K, unpublished
[107] Platow W, Anisimov A N, Dunifer G L, Farle M and Baberschke K 1998 *Phys. Rev.* B **58** 5611
[108] Vonsovskii S V 1966 *Ferromagnetic Resonance* (Oxford: Pergamon)
[109] Sasaki Y 2002 *PhD Dissertation* University of Notre Dame, unpublished
[110] Chappert C, Le Dang K, Beauvillian P, Hurdequint H and Renard D 1986 *Phys. Rev.* B **34** 3192
[111] Cochran J F, Rudd J M, From M, Heinrich B, Bennett W, Schwarzacher W and Egelhoff W F 1992 *Phys. Rev.* B **45** 4676
[112] Sinova J, Jungwirth T, Liu X, Sasaki Y, Furdyna J K, Atkinson W A and MacDonald A H 2004 *Phys. Rev.* B **69** 085209
[113] Kirby B J, Borchers J A, Rhyne J J, te Velthuis S G E, Hoffmann A, O'Donovan K V, Wojtowicz T, Liu X, Lim W L and Furdyna J K 2004 *Phys. Rev.* B **69** 081307(R)
[114] Kittel C and Mitchell A H 1956 *Phys. Rev.* **101** 1611
Mitchell A H 1957 *Phys. Rev.* **105** 1439
[115] Jungwirth T, Sinova J, Wang K Y, Edmonds K W, Campion R P, Gallagher B L, Foxon C T, Niu Q and MacDonald A H 2003 *Appl. Phys. Lett.* **83** 320
[116] Kambersky V, Heinrich B and Fraitová D 1966 *Phys. Lett.* **23** 26